Taylor & Francis
Taylor & Francis Group

Subgrid-scale dynamics and model test in a turbulent stratified jet with coexistence of stable and unstable stratification

Duo Xu[a] and Jun Chen

School of Mechanical Engineering, Purdue University, West Lafayette, IN, USA

ABSTRACT

The subgrid-scale dynamics of stratified flows is studied in a horizontally introduced turbulent jet with coexistence of stable and unstable stratification of a low Richardson number case and a high Richardson number case. The positive production of subgrid-scale kinetic energy and the production of scalar variance suggest the forward energy cascade. The subgrid-scale buoyant destruction plays a role as a sink of subgrid-scale kinetic energy in the stable stratification while holds a role of turbulent generation in the unstable stratification. The role-switch of buoyant destruction in the stable stratification of high-*Ri* case implies the occurrence of a destabilising process triggered by the coupled instability mechanisms. The energy balance assumption related to the production of and the dissipation of subgrid-scale kinetic energy as well as the subgrid-scale buoyant destruction may fail. The *a-priori* test suggests the scale-invariant dynamic and standard Smagorinsky models not to work properly here, while the scale-dependent dynamic model gives a decent performance but with restrictions of the ratio between two testing filter scales.

1. Introduction

Fundamental understanding of stratified flows is of significance in engineering applications, oceanography, environmental and atmospheric science.[1–3] The interactions of turbulence with scalar (density or temperature) interfaces often influence the development of oceanic flows and atmospheric shear layers. These geophysical flows involve high Reynolds number turbulent flows covering a wide range of length scales, in which the associated heat and mass transfer need to be modelled accurately in various numerical studies.[4,5] The traditional Reynolds-averaged Navier–Stokes (RANS) approach with the second-order turbulent models has been employed extensively [e.g., 6,7] but obtained unsatisfactory predictions of unsteady flows. RANS approach still remains a necessity in modelling weather and climate due to its economical computational costs. On the other side, large-eddy simulation (LES) has been widely applied to study oceanic flows and atmospheric boundary layers (ABL),[8–10] bottom boundary layers under oscillating tidal currents [11], and

---

CONTACT Duo Xu ✉ duo.xu@fau.de
[a] Present address: Friedrich-Alexander-Universität Erlangen-Nürnberg, 91058 Erlangen, Germany.

bottom-propagating compositional gravity currents,[12] as well as the planetary boundary layer involved with varieties of physical processes.[13,14] LES yields improved predictions because turbulent eddies at scales equal or larger than numerical grid sizes are explicitly resolved while features at smaller scales are modelled. With the capability of capturing physical features under (weakly) stable conditions,[15] it is still unfortunately challenging in conditions where stratification changes temporally and spatially in a significant way.[16]

The unresolved subgrid-scale (SGS) part of a flow variable f is $f^{SGS}(\mathbf{x}, t) = f(\mathbf{x}, t) - \widetilde{f}(\mathbf{x}, t)$, where $\widetilde{f}(\mathbf{x}, t) = \int_D G_\Delta(\mathbf{r}) f(\mathbf{x} - \mathbf{r}, t) d\mathbf{r}$ is the resolved part (G_Δ is a filtering kernel with a scale of Δ and D the computational domain). In LES of stratified turbulence, the presence of SGS stresses $\tau_{ij}^\Delta = \widetilde{u_i u_j} - \tilde{u}_i \tilde{u}_j$ and SGS scalar fluxes $q_j^\Delta = \widetilde{u_j \theta} - \tilde{u}_j \tilde{\theta}$ (where $\theta = \Delta\rho/\Delta\rho_0$ is non-dimensional density difference in this study) as additional unknowns necessitates proper SGS models to close the governing equations.[17] With the assumptions of eddy-viscosity-diffusivity, Smagorinsky models relate τ_{ij}^Δ to the resolved strain rate tensor as $\tau_{ij}^{\Delta,mod} - (1/3)\tau_{kk}\delta_{ij} = -2\nu_{SGS}\tilde{S}_{ij}$ where $\tilde{S}_{ij} = (\partial\tilde{u}_i/\partial x_j + \partial\tilde{u}_j/\partial x_i)/2$ is the resolved strain rate tensor, $\nu_{SGS} = (C_s\Delta)^2|\tilde{S}|$ the SGS eddy viscosity, $|\tilde{S}| = (2\tilde{S}_{ij}\tilde{S}_{ij})^{1/2}$ the magnitude of the resolved strain rate tensor, and C_s the Smagorinsky coefficient.[18] SGS scalar fluxes are similarly related to the resolved scalar gradients $q_j^{\Delta, mod} = -\kappa_{SGS}(\partial\tilde{\theta}/\partial x_j)$, where κ_{SGS} is the SGS eddy diffusivity. The SGS turbulent Prandtl number $Pr_{SGS} = \nu_{SGS}/\kappa_{SGS}$ is introduced to bridge momentum transports and the development of scalar fields.[1] Thus, ν_{SGS} (or C_s), κ_{SGS} and Pr_{SGS} are usually specified before simulations, for example, as constants in the standard Smagorinsky model ($C_s = 0.17$ and $Pr_{SGS} = 0.3 \sim 1$).[19,20] An improved approach is to dynamically determine these model coefficients, where C_s and Pr_{SGS} can be obtained during the simulation using a scale-invariant assumption $C_s^{2,\Delta} = C_s^{2,\alpha\Delta}$ by employing a second filtering operation at scale $\alpha\Delta$.[21] Another approach assumes a scale-dependent relationship $C_s^{2,\alpha\Delta} \propto \Delta^\phi$ and needs two test filtering operations at the scale of $\alpha\Delta$ and $\alpha^2\Delta$ to make the power coefficient ϕ solvable.[22,23] A variety of other SGS models were developed for specific applications. Because of the wide use in simulating stratified flows [e.g., 10,12,24,25], the eddy-viscosity-diffusivity models are examined in this study.

Appropriate selections of SGS models are important to achieve realistic simulations especially when turbulence is of strong anisotropy or non-homogeneity.[26–28] Almost all the previous examinations focus on the homogeneous stably stratified turbulence. However, turbulence behaves differently when stratification changes like ABL features diurnal variations; or when the stable and unstable stratification coexist and vary reciprocally, which brings in questions whether the SGS modelling assumption, e.g., $C_s^{2,\Delta} = C_s^{2,\alpha\Delta}$ or $C_s^{2,\alpha\Delta} \propto \Delta^\phi$, remains valid under these conditions, applications of these models require precondition or have limitations, and so on. This motivates our *a-priori* examinations of the SGS models with coexistence of stable and unstable stratification.

The mechanism of kinetic energy transfer from the largest to the smallest scales is inherently important in understanding the fundamental physics of turbulence. Stratified geophysical flows, with the presence of the Coriolis effect, often experience a more complex energy transfer process among various spatio-temporal scales and deviate from the forward energy cascade of isotropic turbulence which satisfies a $-5/3$ scaling law.[29] It relates to general arguments if energy exhibits a forward cascade like homogeneous isotropic turbulence or an inverse cascade as expected from a balanced dynamics.[30] Even when

the rotation effect is negligible, energy transfers in stably stratified flows are still difficult to reach a universal description because of the case dependence caused by its strongly anisotropic features.[17] More theoretical and numerical efforts have been put on interpreting the effects of stratification on turbulent energy cascades.[31,32] In particular, examining stratified turbulence experimentally, which requires the knowledge of velocity and scalar fields simultaneously,[17] remains a technical challenge with limited options. An array of anemometers was applied in the field measurements of ABL with an abundant temporal resolution but a limited spatial resolution.[33] Parts of these measurements focus on the SGS dynamics and the effects of stability on the SGS quantities (e.g., SGS fluxes, modelling coefficients).[34] A general description of SGS turbulence under neutral, convective and stable conditions is found to be possible since they share common turbulent properties.[28] Recent laboratory experiments applied the particle image velocimetry (PIV) combined with the planar laser-induced fluorescence (PLIF) to obtain high-spatial-resolution velocity-scalar data (with often finite temporal sampling rates) in a buoyant jet [35] and turbulent gravity currents.[36] These efforts bring in valuable understandings of stratified flows on either stable stratification conditions or buoyancy driven flows, but rarely provide insights into SGS physics. More importantly, turbulent flows often exist in the alternating stable and unstable stratification or in the coexistence of stable and unstable stratification, which have not been well understood yet to the best of our knowledge. Strong couplings of the velocity field and the scalar field make the characteristic length and temporal scales vary strongly, and lead to different behaviour between stable and unstable stratification, which often challenges the development of effective turbulence models. This motivates our present study of a stratified flow with the coexistence of stable and unstable stratification in laboratory experiments. Our high-spatial-resolution velocity-scalar data (16 K sampling points per snapshot) enable us, in particular, to pursue answers to several key questions: (1) What are the differences in the transfer of kinetic energy and scalar fluxes from resolved to SGS scales in the coexistent stable and unstable stratification? (2) What are the specific roles of buoyancy in the energy cascade in stable and unstable stratification? and (3) Is there any special requirement when simulates similar problems with using dynamic SGS models? To address these questions, this paper is organised as follows: the experimental data-set is introduced in Section 2; Section 3 presents results and discussions and conclusions are drawn in Section 4.

2. Experimental data-set

The experiments are performed in a turbulent jet facility as sketched in Figure 1, where a dense fluid (salt solution, density ρ_s) is injected through a nozzle into a light fluid (ethanol solution, density ρ_e) with a slight density difference (as shown in Table 1 together with other experimental conditions). The main tank is of 110 cm $(L) \times 30$ cm $(H) \times 30$ cm (W). The jet is horizontally introduced, so the dominant momentum direction at the nozzle exit is along the horizontal direction (x_1), perpendicular to the buoyancy direction (x_3). As the jet mixes with the ambient fluid, two different stratification mechanisms are developed: in the upper mixing layer, the dense fluid is below the light fluid to form a stable stratification, which weakens the mixing and entrainment; at the lower mixing layer, the dense fluid is above the light fluid to form an unstable stratification, which enhances the mixing and entrainment.
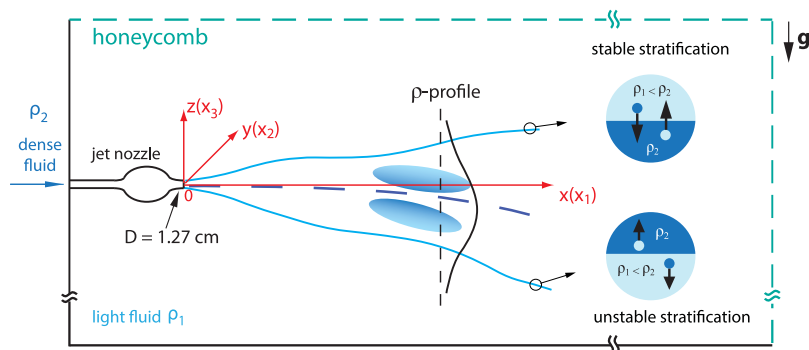
Figure 1. Schematics of the turbulent jet facility, where the stable and unstable stratification are marked in details A and B. Also sketched is a typical profile of the mean density. Arrows in the right plot show the direction of restoring force due to buoyancy when a fluid element is disturbed from its original equilibrium state. The arrow of **g** marks the direction of gravitational acceleration.

Thus, the stratified jet experiments in this study introduce a unique co-existence of stable and unstable stratification.

Simultaneous velocity–density measurements are achieved by combining PIV and PLIF techniques. The dense fluid is uniformly mixed with the fluorescent dye (rhodamine 6G, excitation wavelength 530 nm, emission wavelength 550 nm) for the PLIF measurement. Seeding particles (hollow glass beads, mean diameter 10 μm, specific gravity 1.1) are added into both dense and light fluids. A 1/2 mm thick laser sheet is formed through a group of optical lenses and mirrors to illuminate the central vertical plane $(x_1, 0, x_3)$ of the jet. Two CCD cameras are used to record PIV and PLIF images, respectively. A filter set (a band-pass filter with the centre wavelength 532 nm for PIV and a long pass filter with cut-off wavelength 550 nm for PLIF) is applied to separate the PIV and PLIF images. The scalar field from PLIF is then sub-sampled to match the spatial resolution of the velocity field from the PIV measurement. Before performing measurements, PLIF has to be calibrated to relate the local density to the local concentration of fluorescent dye to achieve quantitative measurements. With detailed error analysis, the characteristic errors of instantaneous

Table 1. Experimental conditions characterised at the nozzle exit of the stratified jet.

Parameter	low-Ri	high-Ri
Nozzle inner diameter D (cm)	1.27	1.27
Inlet velocity $\langle U_0 \rangle$ (m/s)	1.9	0.25
Inlet density difference $\Delta \rho_0/\rho_s = (\rho_s - \rho_e)/\rho_s$	0.5%	0.5%
Inlet turbulent intensity $u_{rms}/\langle U_0 \rangle$	4.5%	3.5%
Inlet Reynolds number $Re_0 = \langle U_0 \rangle D/\nu$	24,000	3,200
Inlet bulk Richardson number $Ri_b = \Delta \rho_0 Dg/(\rho_s \langle U_0 \rangle^2)$	0.0002	0.01
Estimated dissipation rate $\epsilon = u_{rms}^3/D$ (m^2/s^3)	0.11	0.00004
Kolmogorov scale $\eta_k = (\nu^3/\epsilon)^{1/4}$ (mm)	0.05	0.38
Batchelor scale $\eta_b = \eta_k/\sqrt{Sc}$ (mm)	0.002	0.016
PIV resolution δ_v (mm)	$0.86 \simeq 17\eta_k$	$0.89 \simeq 2.4\eta_k$
PLIF resolution δ_θ (mm)	$0.054 \simeq 18\eta_b$	$0.056 \simeq 3.5\eta_b$
Schmidt number[a] $Sc = \nu/D_c$ (D_c: mass diffusivity)	$500 \sim 700$	$500 \sim 700$

Analogue of Prandtl number $Pr = \nu/\alpha$ in heat transfer (α: thermal diffusivity).
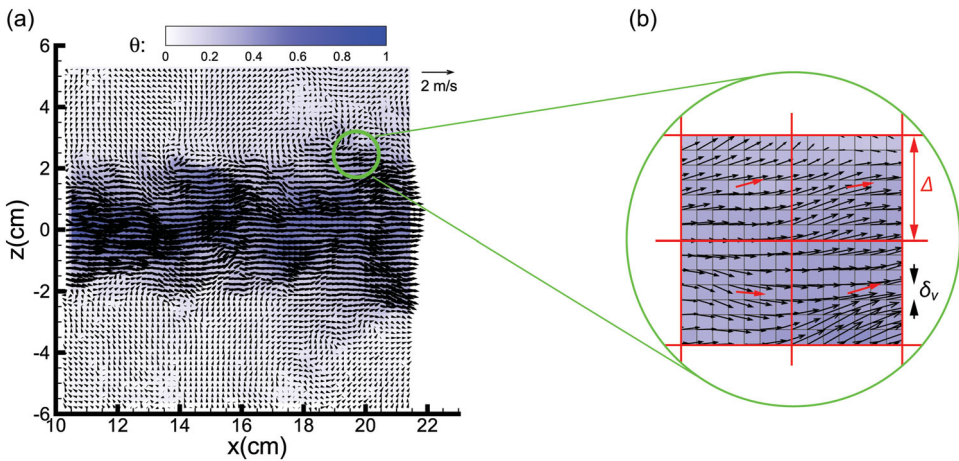
Figure 2. A paired snapshot sample of simultaneous velocity (vector) and non-dimensional density difference θ (contour) fields is shown in (a). Only 1/4 of the velocity vectors are plotted for clarity of display. The vectors and scalar contour within the green circle are zoomed in (b) with the LES filter scale Δ and PIV resolution δ_v marked as well as filtered velocity field indicated by the red arrows.

measurements are 0.7% for velocity and 2% for scalar in this study. The measurement technique, PLIF calibration approach, and uncertainty analysis, as well as other experiment related information, have been introduced in detail in another publication.[37] A snapshot of instantaneous velocity and density fields on a resolved 128×128 grid is shown in Figure 2. Data from two sets of experiments are presented in this study, as summarised in Table 1. The first set, labelled as 'low-Ri' case, has an inlet velocity $\langle U_o \rangle = 1.9$ m/s with 0.5% density difference, where the bulk Richardson number is 0.0002. The second set ('high-Ri' case) has a smaller inlet velocity $\langle U_o \rangle = 0.25$ m/s with a bulk Richardson number of 0.01. For the low-Ri case, measurements are conducted at three consecutive downstream frames spanning from $x/D = 0$ to 25. The field of view for each frame is 11×11 cm^2. For the high-Ri case, measurements are conducted at two consecutive frames ($x/D = 0$ to 18.5). Under each experimental condition, large amounts of instantaneous snapshots (600 for the low-Ri case and 2000 for the high-Ri case) are collected for converged statistical analysis.

In the following analysis, $\langle \cdot \rangle$ represents an ensemble averaging operation. The mean streamwise velocity and density distributions are plotted in Figure 3, where $\theta(x, y)$ is the non-dimensional density distribution ($0 \le \theta \le 1$. $\theta = 0$: light fluid; $\theta = 1$: dense fluid). As shown in Figure 3, buoyancy effect is relatively weak in the low-Ri case, while it is stronger in the high-Ri case by bending the jet towards the gravity direction at downstream locations. To highlight the buoyancy effect, data from the well-developed downstream jet regions (as enclosed by the red rectangles in Figure 3) are used to investigate the SGS stratified turbulence.

3. Results

In the following analysis, a spatial two-dimensional top-hat (box) filter is applied to the experimentally acquired velocity–density data to obtain their resolved and unresolved parts as defined. The filter width corresponds to a length scale separating the resolved and SGS
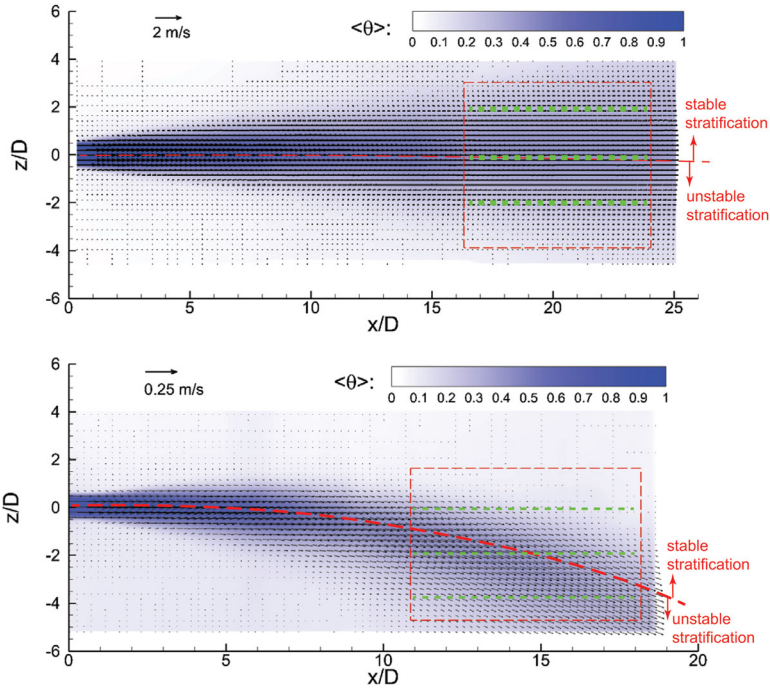
Figure 3. Development of the mean density $\langle\theta\rangle$: (top) low-*Ri* case and (bottom) high-*Ri* case. The vectors represent the mean velocity field. Only 1/9 of the velocity vectors are plotted for clarity of display. The red rectangles enclose the data used for the statistical analysis in this study. The dashed green lines mark the locations where the velocity data are used to spectral analysis.

quantities. The adopted filter scales are also marked in Figure 4 with one-dimensional kinetic energy spectra $E_{11}(k_1)$ and $E_{33}(k_1)$. The spectra are computed by applying the Fourier transform to velocity fluctuation components obtained from the Reynolds decomposition ($u'_j = u_j - \langle u_j\rangle, j = 1, 3$) along the x_1 direction. One may refer to, e.g., [38], for procedures of spectral analysis using the PIV data. In particular, these spectra are compared to their counterparts with the same Reynolds number but no stratification ($\Delta\rho_0 = 0$ g/L, titled as 'high-*Re*' and 'low-*Re*' cases, respectively). From the spectra of the low-*Ri* case, the filter scale $\Delta/\delta_v = 4$ (where δ_v is the PIV spatial resolution) falls into the dissipation range, while the scales of $\Delta/\delta_v = 8 \sim 28$ are approximately in the inertial range. $\Delta/\delta_v = 4$ in the high-*Ri* case locates in the dissipation range and $\Delta/\delta_v = 8 \sim 20$ are within the inertial range. These filter scales are chosen to cover the dissipation range and the inertial range of the corresponding case.

In this study, the derivatives of velocity are evaluated using a least-squares filter through five neighbouring points on the PIV grid, i.e.,

$$\frac{\partial u_i}{\partial x_j}\bigg|_{(m,n)} = \frac{-2u_i|_{(m,n-2)} - u_i|_{(m,n-1)} + u_i|_{(m,n+1)} + 2u_i|_{(m,n+2)}}{10\delta_v}, \tag{1}$$
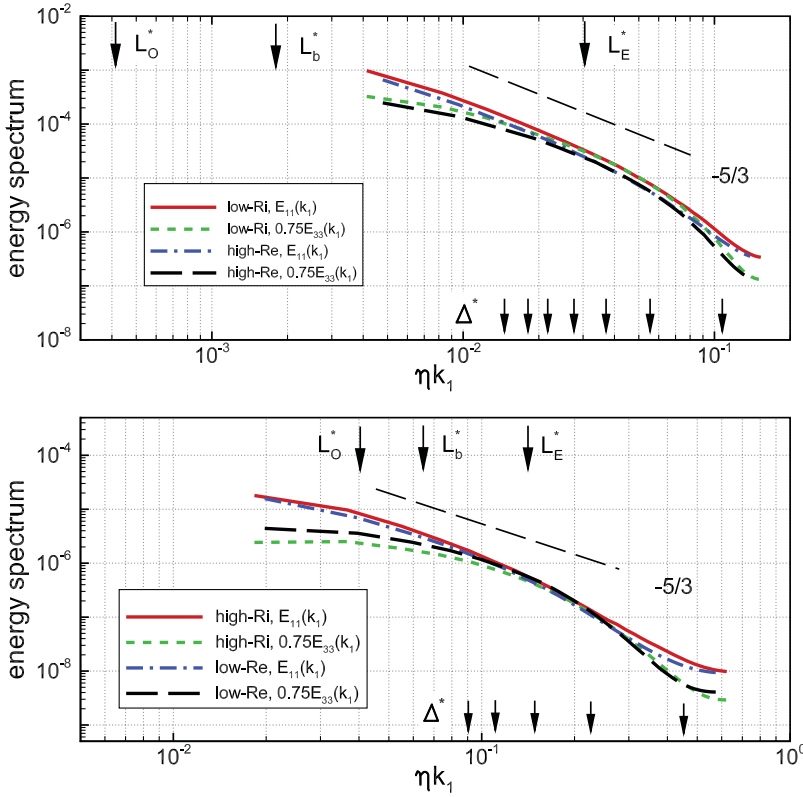
Figure 4. One-dimensional spectra, $E_{11}(k_1)$ and $E_{33}(k_1)$, of the low-Ri case (top) and the high-Ri case (bottom), and comparisons with their counterparts in unstratified high-Re (Re_0=24,000, $Ri_b = 0$) and low-Re ($Re_0 = 3200$, $Ri_b = 0$) cases. The vertical arrows mark the scales of different LES filters $\Delta^* = 2\pi\eta/\Delta$ used in this study, i.e., corresponding to Δ/δ_v=28, 24, 20, 16, 12, 8, 4 from left to right for the low-Ri case, and corresponding to Δ/δ_v=20, 16, 12, 8, 4 from left to right for the high-Ri case. The spectra are computed using the data at $z/D = 0$ for the low-Ri case and $z/D = -2$ for the high-Ri case, as marked in Figure 3. Data from five neighbouring horizontal lines are averaged. In addition, the length scales $L_O^* = 2\pi\eta/L_O$, $L_b^* = 2\pi\eta/L_b$ and $L_E^* = 2\pi\eta/L_E$ are also marked by arrows.

to reduce the error of derivative evaluation using the PIV data.[38] Similarly, the derivatives of scalar are evaluated by

$$\frac{\partial\theta}{\partial x_j}\bigg|_{(m,n)} = \frac{-2\theta|_{(m,n-2)} - \theta|_{(m,n-1)} + \theta|_{(m,n+1)} + 2\theta|_{(m,n+2)}}{10\delta_\theta}, \tag{2}$$

where δ_θ is the PLIF pixel resolution (Table 1). The quality of the five-point discrete derivative algorithm is examined by following an approach reported in [39] and [28], which examines the error of calculating the divergence-free condition of the resolved velocity field ($\partial\tilde{u}_i/\partial x_i = 0$). An evaluation of the quality of the five-point discrete derivation in this study is detailed in Appendix 1.

The transport equation of the SGS part of kinetic energy, $k_{SGS} = (\widetilde{u_i u_i} - \tilde{u}_i \tilde{u}_i)/2$ is presented in [17]. With an ensemble averaging operation, one has

$$\frac{\partial \langle k_{SGS} \rangle}{\partial t} + \left\langle \tilde{u}_j \frac{\partial k_{SGS}}{\partial x_j} \right\rangle + \frac{\partial \langle T_i \rangle}{\partial x_i} = \langle \Pi^\Delta \rangle - \langle B_{SGS}^\Delta \rangle - \langle \epsilon_{SGS}^\Delta \rangle, \tag{3}$$

where $\langle T_i \rangle = \langle (\widetilde{u_i u_j u_j} - \tilde{u}_i \widetilde{u_j u_j})/2 + \nu(\tilde{u}_j \widetilde{S}_{ij} - \widetilde{u_j S_{ij}}) + 2(\widetilde{p u_j} - \tilde{p} \tilde{u}_j)\delta_{ij}/\rho - \tilde{u}_j \tau_{ij}^\Delta \rangle$ represents the mean transportation of SGS motions. $\langle \epsilon_{SGS}^\Delta \rangle = 2\nu \langle \widetilde{S_{ij} S_{ij}} - \widetilde{S}_{ij} \widetilde{S}_{ij} \rangle$ is the viscous dissipation of the SGS kinetic energy. $\langle \Pi^\Delta \rangle = -\langle \tau_{ij}^\Delta \widetilde{S}_{ij} \rangle$ is the rate of production of SGS kinetic energy,[29] which is also called the SGS dissipation of kinetic energy to represent a sink of the resolved kinetic energy into unresolved scales [27] (we do not differentiate them here). $\langle B_{SGS}^\Delta \rangle = g'\langle \widetilde{\theta u_3} - \tilde{\theta} \tilde{u}_3 \rangle$ represents the SGS buoyant destruction. Similarly, the transport equation of the SGS part of scalar variance, $\zeta_{SGS} = (\widetilde{\theta^2} - \tilde{\theta}^2)/2$, is given by

$$\frac{\partial \langle \zeta_{SGS} \rangle}{\partial t} + \left\langle \tilde{u}_j \frac{\partial \zeta_{SGS}}{\partial x_j} \right\rangle + \frac{\partial \langle Q_j \rangle}{\partial x_j} = \langle \chi^\Delta \rangle - \Gamma \left\langle \widetilde{\frac{\partial \theta}{\partial x_j} \frac{\partial \theta}{\partial x_j}} - \frac{\partial \tilde{\theta}}{\partial x_j} \frac{\partial \tilde{\theta}}{\partial x_j} \right\rangle, \tag{4}$$

where $\langle Q_j \rangle = \langle \widetilde{\theta^2 u_j} - \tilde{\theta}^2 \tilde{u}_j - 2\tilde{q}_j \tilde{\theta} - \Gamma \partial(\widetilde{\theta^2} - \tilde{\theta}^2)/\partial x_j \rangle/2$ with molecular diffusivity Γ. $\langle \chi^\Delta \rangle = -\langle q_j^\Delta (\partial \tilde{\theta}/\partial x_j) \rangle$ serves analogously as the production of ζ_{SGS} (also interpreted as the sink of resolved scalar variance into SGS). $\Gamma \langle \widetilde{(\partial \theta/\partial x_j)(\partial \theta/\partial x_j)} - (\partial \tilde{\theta}/\partial x_j)(\partial \tilde{\theta}/\partial x_j) \rangle$ is the dissipation of ζ_{SGS} due to molecular diffusivity.

Various length scales are associated with stratified turbulence to quantify the local flow characteristics, such as the Ozmidov length scale

$$L_O = \left(\frac{\epsilon}{N^3} \right)^{1/2}, \tag{5}$$

indicates the upper limit of the isotropic three-dimensional turbulence in stratified fluids,[40,41] where $\epsilon = \nu \langle (\partial u_i'/\partial x_j)(\partial u_i'/\partial x_j) + (\partial u_i'/\partial x_j)(\partial u_j'/\partial x_i) \rangle$ is the viscous dissipation of turbulent kinetic energy and $N = \sqrt{(g\Delta\rho_0/\rho_s)|\partial \langle \theta \rangle/\partial x_3|}$ the Brunt–Väisälä frequency. The buoyancy length scale

$$L_b = \frac{k^{1/2}}{N}, \tag{6}$$

where $k = \langle u_i' u_i' \rangle/2$ is the turbulent kinetic energy, corresponds to the thickness of shear layers in stratified turbulence.[42] The different dependence of L_O and L_b on N implies the distinct physical processes.[43] In addition, the Ellison length scale,

$$L_E = \frac{|\langle \theta'^2 \rangle|^{1/2}}{\partial \langle \theta \rangle/\partial x_3}, \tag{7}$$

estimates the overturning eddy size, where $\theta' = \theta - \langle \theta \rangle$ is the density fluctuation in Reynolds decomposition. To quantify the local competition between the buoyancy effect
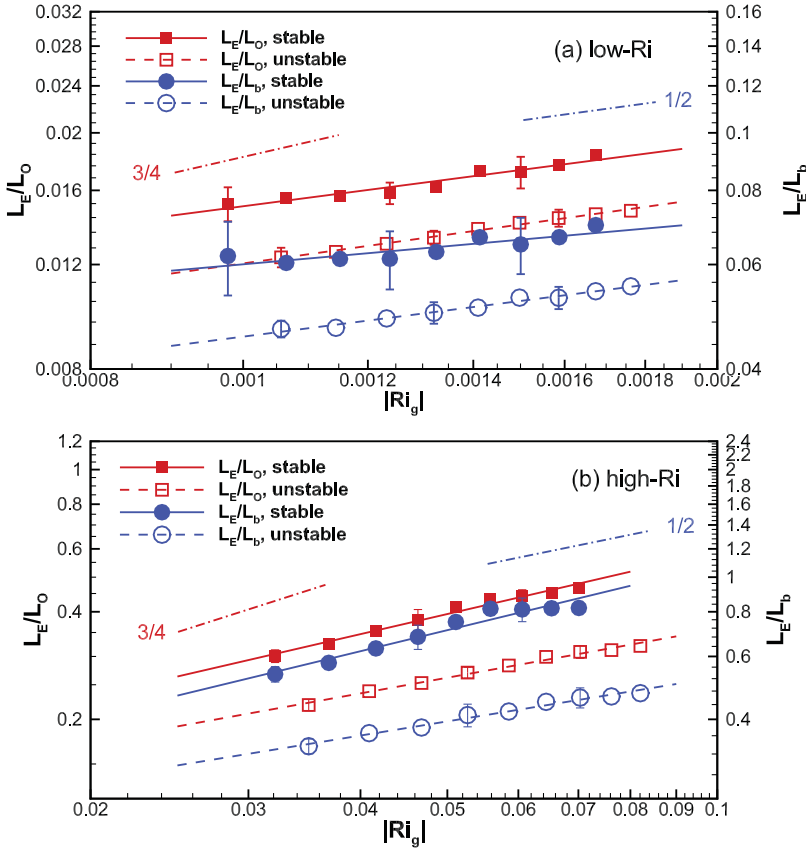
Figure 5. The dependence of L_E/L_O and L_E/L_b on $|Ri_g|$, with a power-law fitting to guide the eyes. The errorbars indicate the standard deviations. The axes are in log-scale. The red dashed–dotted line marks the slope of 3/4 referring to the L_E/L_O axis, and the blue dashed–dotted line marks the slope of 1/2 referring to the L_E/L_b axis.

and inertial effect, the gradient Richardson number

$$Ri_g = -g' \frac{\partial \langle \theta \rangle / \partial x_3}{(\partial \langle u_1 \rangle / \partial x_3)^2}, \tag{8}$$

is often introduced, where $g' = g\Delta\rho_0/\rho_s$ is the reduced gravity and g is the gravitational acceleration. In this study, the local bulk Richardson number is also introduced as

$$Ri_b = \frac{g'\langle\theta\rangle L_O}{\langle u_1 \rangle^2 + \langle u_3 \rangle^2}, \tag{9}$$

where L_O is the featured size of parcels of fluids, inside which the buoyancy effect is assumed to be trivial. To quantify the local energy cascade, the length scale ratios L_E/L_O and L_E/L_b are often investigated and associated with local stratification quantities, such as Ri_g. For example, an empirical estimate of $L_E/L_O \simeq 4.2Ri_g^{3/4}$ and $L_E/L_b \simeq 1.6Ri_g^{1/2}$ was introduced,[44] which collapsed well with other studies.[45–47] In general, as shown in Figure 5, the scale

ratios, in this study, increase as Ri_g increases. For instance, in the high-Ri case, L_E/L_O from this study (stratified jet) agrees with the empirical predictions, and L_E/L_b is larger than the empirical result and approaching the result in [48], where a simplified quasi-equilibrium second-moment closure turbulence model inherited to the Mellor–Yamada model [49] was used.

### 3.1. Rate of production of SGS kinetic energy and of SGS scalar variance

Investigating the rate of production of SGS kinetic energy $\langle \Pi^\Delta \rangle$ and the rate of production of SGS scalar variance $\langle \chi^\Delta \rangle$ provides insights into the turbulence of stratified flows, which elucidates the cascade of kinetic energy and scalar variance over the spectrum of length scales. The measurements are done in the central vertical $x_1 - x_3$ plane ($x_2 = 0$), so from symmetry, one may have $\partial \langle u_j \rangle / \partial x_2 = 0$ and $\partial \langle \theta \rangle / \partial x_2 = 0$. Moreover, the unmeasured terms in $\langle \Pi^\Delta \rangle$ and $\langle \chi^\Delta \rangle$ are therefore assumed small. In this study, $\langle \Pi^\Delta \rangle$ is evaluated using all measurable elements from the PIV data (similar to the surrogate used in [38]):

$$\langle \Pi^\Delta \rangle \simeq -\langle \tau_{11}^\Delta \widetilde{S}_{11} \rangle - 2\langle \tau_{13}^\Delta \widetilde{S}_{13} \rangle - \langle \tau_{33}^\Delta \widetilde{S}_{33} \rangle. \tag{10}$$

Similarly, $\langle \chi^\Delta \rangle$ is calculated by

$$\langle \chi^\Delta \rangle \simeq -\langle q_1^\Delta (\partial \widetilde{\theta}/\partial x_1) \rangle - \langle q_3^\Delta (\partial \widetilde{\theta}/\partial x_3) \rangle. \tag{11}$$

Typical profiles of $\langle \Pi^\Delta \rangle$ and $\langle \chi^\Delta \rangle$ for the low-Ri and high-Ri cases are shown in Figure 6, where the data in stable and unstable stratification are marked by the hollow and solid symbols, respectively. The stable and unstable stratification are differentiated by the signs ($+$ or $-$) of Ri_g. The abscissa is shown in logarithmic scales to clearly illustrate the difference between the data at larger scales (triangle) and smaller scales (circle), as well as the difference between the data at upstream locations (red) and downstream locations (blue). A positive $\langle \Pi^\Delta \rangle$ (or $\langle \chi^\Delta \rangle$) implies an overall forward energy transfer from resolved scale to SGS. The difference of $\langle \Pi^\Delta \rangle$ (or $\langle \chi^\Delta \rangle$) when using large and small filter scales shows the different net rate of kinetic energy transfer, which is larger at the scales locating in the inertial range than that at the scales locating in the dissipation range. More interestingly, $\langle \Pi^\Delta \rangle$ and $\langle \chi^\Delta \rangle$ of the low-Ri case give similar trends that two peaks exist at both the upstream and downstream locations, and the two peaks locate nearly where the maximum velocity gradient along the z-direction occurs, which may suggest that the distributions of $\langle \Pi^\Delta \rangle$ (or $\langle \chi^\Delta \rangle$) are governed by the dominant shear momentum along the z-direction (i.e., $\partial \langle u_1 \rangle / \partial x_3$ and $\partial \langle \theta \rangle / \partial x_3$). However, the two peaks of $\langle \Pi^\Delta \rangle$ (or $\langle \chi^\Delta \rangle$) only exist at the upstream location of the high-Ri case where the momentum suppresses the buoyancy effect, but disappear in its unstable stratification region at the downstream location where the buoyancy effect is significant, which is because the peak of $\partial \langle u_1 \rangle / \partial x_3$ (or $\partial \langle \theta \rangle / \partial x_3$) is smoothed by the streamwise shear, in addition to the increased vertical shear momentum. In addition, in the unstable stratification of high-Ri case, the vertical velocity component is so significant that turbulence becomes anisotropic with a preference along the buoyancy direction. Thus, the vertical stress (and scalar flux) increases to be comparable to (or overcome) the streamwise stress (and scalar flux). It contributes to the increase of vorticity (e.g., Ω_2 in plane $x_2 = 0$) and the enhanced mixing. However, in the stable stratification region, the
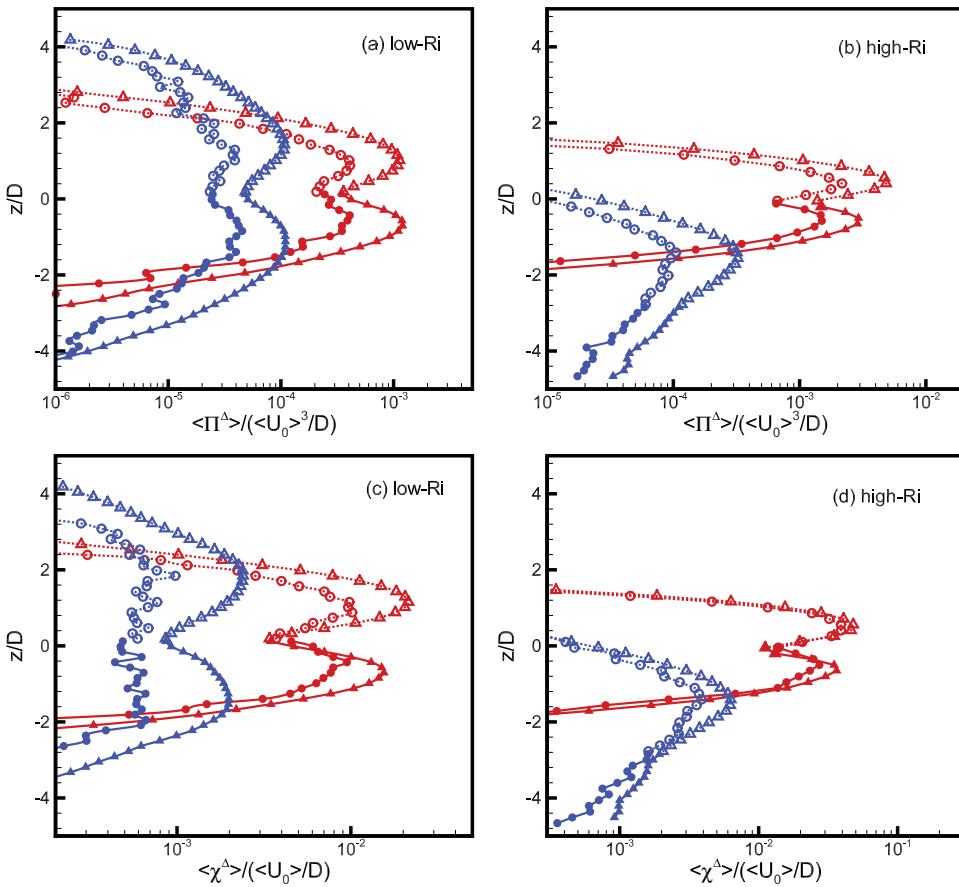
Figure 6. Profiles of $\langle \Pi^\Delta \rangle$ (top panel) and $\langle \chi^\Delta \rangle$ (bottom panel) at two streamwise locations with two filter scales: low-Ri case (a, c) with $\Delta/\delta_v = 4$ (circle) and $\Delta/\delta_v = 20$ (triangle) at $x/D = 10$ (red) and $x/D = 20$ (blue); high-Ri case (b, d) with $\Delta/\delta_v = 4$ (circle) and $\Delta/\delta_v = 12$ (triangle) at $x/D = 5$ (red) and $x/D = 15$ (blue). The hollow symbols represent the data in the stable stratification and the solid symbols represent the data in the unstable stratification. Every other points are shown for clarity.

buoyancy effect suppresses the vertical stress (and scalar flux), where the anisotropic turbulence is of a preference along the streamwise direction. This can be also shown in the one-dimensional velocity spectrum in Figure 7. It is not surprising to see that the velocity spectra of the low-Ri case from the stable and unstable stratification are similar and nearly overlapped with each other ($0.75E_{33}(k_1) \approx E_{11}(k_1)$ in the inertial subrange), indicating that the turbulence is nearly isotropic. Using the spectra of the low-Ri case as a reference, the spectra of high-Ri case from the stable stratification slightly deviate from the reference where a gap exists between $E_{11}(k_1)$ and $0.75E_{33}(k_1)$, implying that the vertical kinetic energy is suppressed at large scales corresponding to the wavenumber $k_1 < 0.1/\eta_k$. Meanwhile, in the unstable stratification region, $0.75E_{33}(k_1)$ is larger than $E_{11}(k_1)$ with a plateau around $\eta_k k_1 = 0.1$, which implies that around this wave-number the contribution of vertical component to the kinetic energy is distinctly increased. The vertical scalar flux stimulates the growth of vertical kinetic energy to form a potentially positive feedback for the
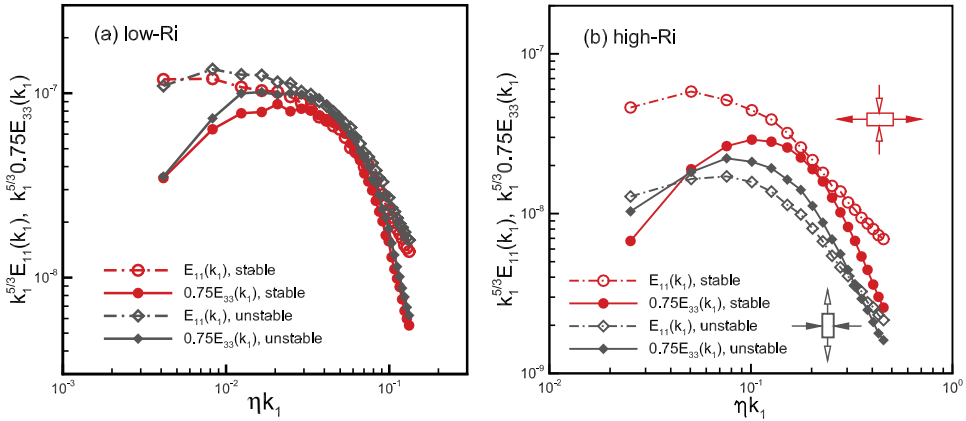
Figure 7. One-dimensional kinetic energy spectra $E_{11}(k_1)$ and $0.75E_{33}(k_1)$ compensated by $k_1^{5/3}$ in the stable and unstable stratification regions, respectively: (a) the low-*Ri* case, where the data at $z/D = \pm 2$, as marked in Figure 3, are used. (b) the high-*Ri* case, where the data at $z/D = 0$ and $z/D = -4$, as marked in Figure 3, are used. The hollow arrows in (b) represent the gravity and buoyancy effects (along the x_3 direction) to compress or elongate a parcel of fluid, and solid arrows represent the momentum (along the x_1 direction) to compress or elongate the same parcel of fluid.

formation of anisotropic turbulence in this region. Additionally, the entire curve of $0.75E_{33}(k_1)$ shifts to the higher end with a prominence from $\eta_k k_1 = 0.05$ to $\eta_k k_1 = 0.3$, indicating that growth of vertical velocity favours at these corresponding length scales. The spectra of stable stratification region are above that of the unstable stratification regions. They suggest the span of the locally integral length scale and the local Kolmogorov length scale in the stable stratification to be wider than that in the unstable one.

　　To study the variations of $\langle \Pi^\Delta \rangle$ (or $\langle \chi^\Delta \rangle$) on scales, the spatially averaged $\langle \Pi^\Delta \rangle$ (or $\langle \chi^\Delta \rangle$) is calculated using the data in the enclosed regions of Figure 3 at different filter scales in stable and unstable stratification separately. In these regions, there are more effective (rather than the background noise) data points that result in a converged statistical analysis. As another objective of this study, the buoyancy effect (relatively comparable to the momentum effect) can be highlighted in these regions as well. As shown in Figure 8, the positive mean of $\langle \Pi^\Delta \rangle$ (or $\langle \chi^\Delta \rangle$) of the low-*Ri* case at either the stable or the unstable stratification increases as Δ increases and asymptotically approach a constant value at large Δ's, indicating a steady energy transfer (in the sense of statistical mean) from resolved scale to SGS in inertial subrange. In particular, the curves from both the stable and unstable stratification nearly collapse due to the weak buoyancy effect. In addition, the small deviation (shown by the error bar) at small scales (e.g., $\Delta/\delta_\nu = 4$) implies the turbulence characteristics is relatively homogeneous at this scale. However, in the stable stratification of the high-*Ri* case, the spatial mean of $\langle \Pi^\Delta \rangle$ (or $\langle \chi^\Delta \rangle$) first increases with Δ and then approaches constants. The large deviations (errorbars) indicate the presence of relatively scattered distributions in this region. It is interesting to discover that in the unstable stratification region $\langle \Pi^\Delta \rangle$ (or $\langle \chi^\Delta \rangle$) reaches a plateau centred at $\Delta/\delta_\nu = 12$, which is contributed by the vertical momentum (or scalar) flux at such length scales (corresponding to $\eta_k k_1 \simeq 0.1$ in Figure 7).

　　Another indispensable question is whether the distribution of $\langle \Pi^\Delta \rangle$ (or $\langle \chi^\Delta \rangle$) depends on the local stratification quantity. The introduced local bulk Richardson number Ri_b
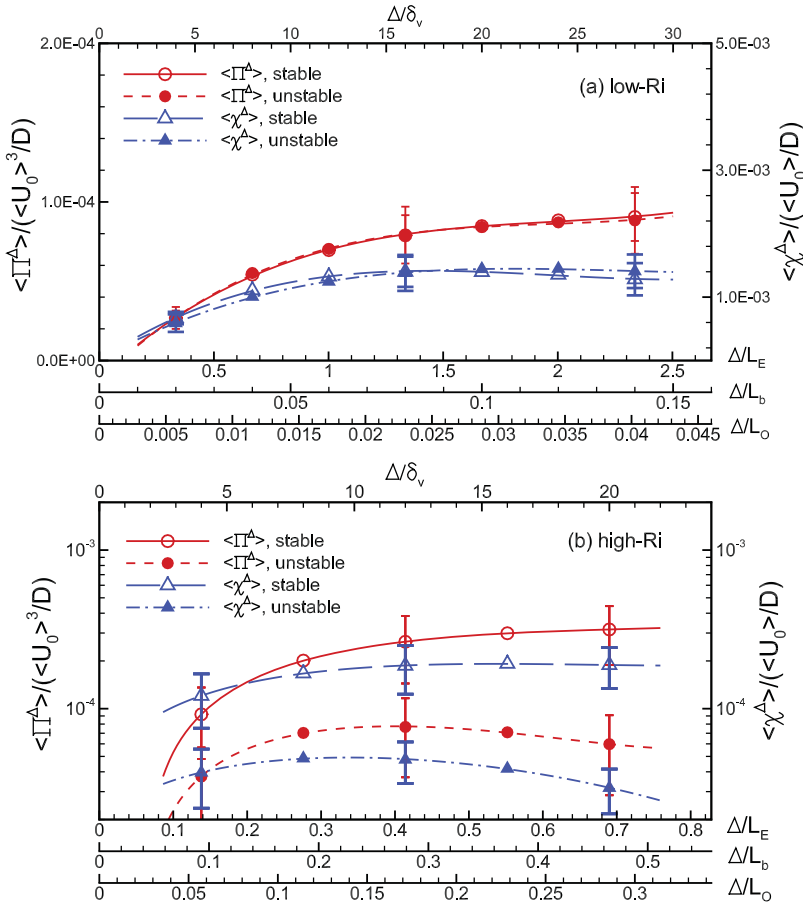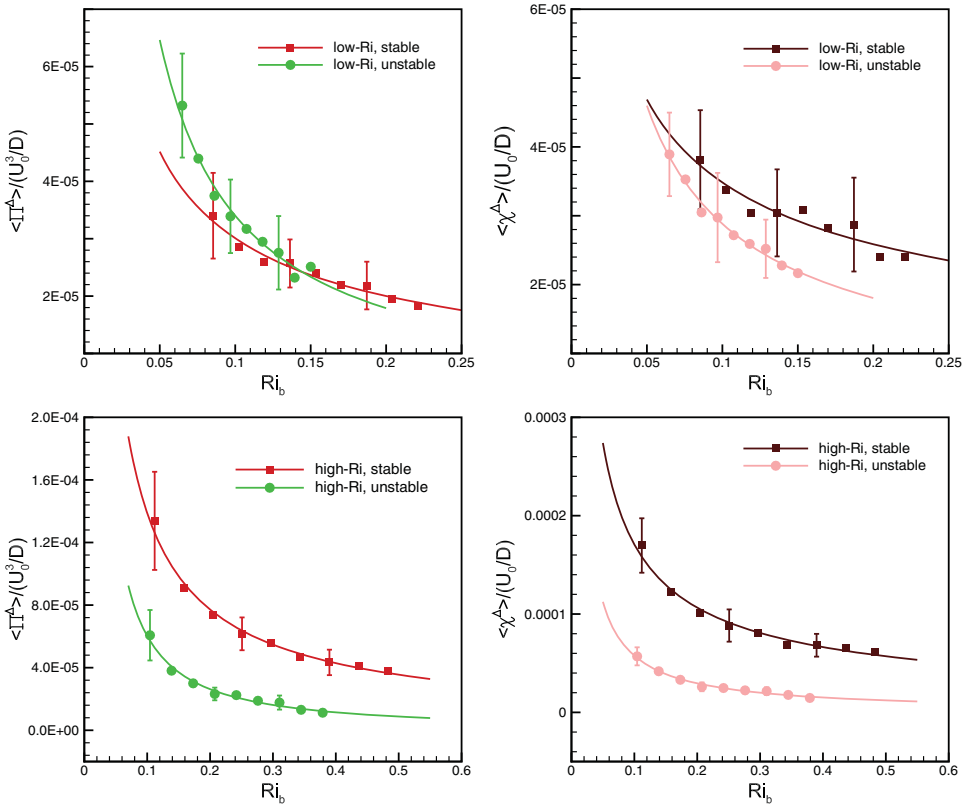
Figure 8. The spatially averaged mean of $\langle\Pi^\Delta\rangle$ and χ^Δ at each scale are plotted against filter scales (from $\Delta/\delta_v = 4$ to $\Delta/\delta_v = 28$) for different stratification regions of the low-*Ri* case (top) and the high-*Ri* case (bottom). The red symbols (squares and circles) correspond to $\langle\Pi^\Delta\rangle$ on the left ordinate axis, while blue symbols (triangles and diamonds) correspond to $\langle\chi^\Delta\rangle$ on the right ordinate axis. The error bars show their standard deviations. The abscissas of Δ normalised by L_O, L_b and L_E are shown, respectively.

(Equation (9)) is ideal to quantify the local stratification through comparing the buoyancy and inertia effects. The conditional mean of $\langle\Pi^\Delta\rangle$ (or $\langle\chi^\Delta\rangle$) on Ri_b is calculated within the stable and unstable stratification regions separately at the studied filter scales. For clarity, Figure 9 only shows $\langle\Pi^\Delta\rangle$ (or $\langle\chi^\Delta\rangle$) on Ri_b at one filter scale $\Delta/\delta_v = 4$. The power-fit of the data points captures the decreasing trend of $\langle\Pi^\Delta\rangle$ (or $\langle\chi^\Delta\rangle$) as Ri_b, which implies that the SGS production terms are mainly contributed by the inertia effect rather than the buoyancy effect.

### 3.2. Subgrid-scale buoyant destruction and energy balance

When the stratified turbulence reaches a statistically steady state, $\partial\langle k_{SGS}\rangle/\partial t$ vanishes, Equation (3) turns to represent the energy balance among the remaining terms, i.e.,

$$\langle\Pi^\Delta\rangle - \langle B^\Delta_{SGS}\rangle - \langle\epsilon^\Delta_{SGS}\rangle - \partial\langle T_i\rangle/\partial x_i - \langle\tilde{u}_j\partial k_{SGS}/\partial x_j\rangle \simeq 0. \tag{12}$$

Figure 9. The dependence of $\langle \Pi^\Delta \rangle$ (left panel) and $\langle \chi^\Delta \rangle$ (right panel) on Ri_b in the stable and unstable stratification regions of the low-*Ri* case (top) and the high-*Ri* case (bottom). The data of $\Delta/\delta_v = 4$ are shown for clarity. The curves are from power-law fitted data. The error bars correspond to the standard deviations.

The SGS buoyant destruction is thus expected to play an important role in the evolution of SGS kinetic energy. For instance, in the stable stratification region, $\langle \Pi^\Delta \rangle$ serves as a source to produce the SGS kinetic energy, while $\langle B_{SGS}^\Delta \rangle$ and $\langle \epsilon_{SGS}^\Delta \rangle$ as sinks to consume it, but in the unstable stratification, $\langle B_{SGS}^\Delta \rangle$ switches its role to a source despite $\langle \Pi^\Delta \rangle$ and $\langle \epsilon_{SGS}^\Delta \rangle$ remain their roles. With the understanding of the variations of $\langle \Pi^\Delta \rangle$ upon the filter scales (shown in Figure 8), a key concern is to understand how $\langle B_{SGS}^\Delta \rangle$ varies with Δ's. Figure 10 shows that $\langle B_{SGS}^\Delta \rangle$ varies almost linearly against Δ's in both the stable and unstable stratification regions of the low-*Ri* case as well as the unstable stratification of the high-*Ri* case. This indicates that a fixed percentage of $\langle B_{SGS}^\Delta \rangle$ has been consumed among the scales, e.g., about 4% of the buoyancy flux consumed per δ_v in both stratification of the low-*Ri* case and 6% for the unstable stratification of high-*Ri* case, which is dramatically different to the fixed amount of $\langle \Pi^\Delta \rangle$ (or $\langle \chi^\Delta \rangle$) that indicates a preserved kinetic energy cascade rate over the inertial subrange. But $\langle B_{SGS}^\Delta \rangle$ from the stable stratification of high-*Ri* case deviates from the above finding, with a decreasing consumption percentage from large filter scales to small ones. In particular, the buoyant destruction dissipates more quickly at $\Delta > 12\delta_v$ than those at $\Delta < 12\delta_v$. More importantly in this region, rather than a sink, $\langle B_{SGS}^\Delta \rangle$ behaves like a source with large spatial deviation. This role-switch suggests that parts of the stable
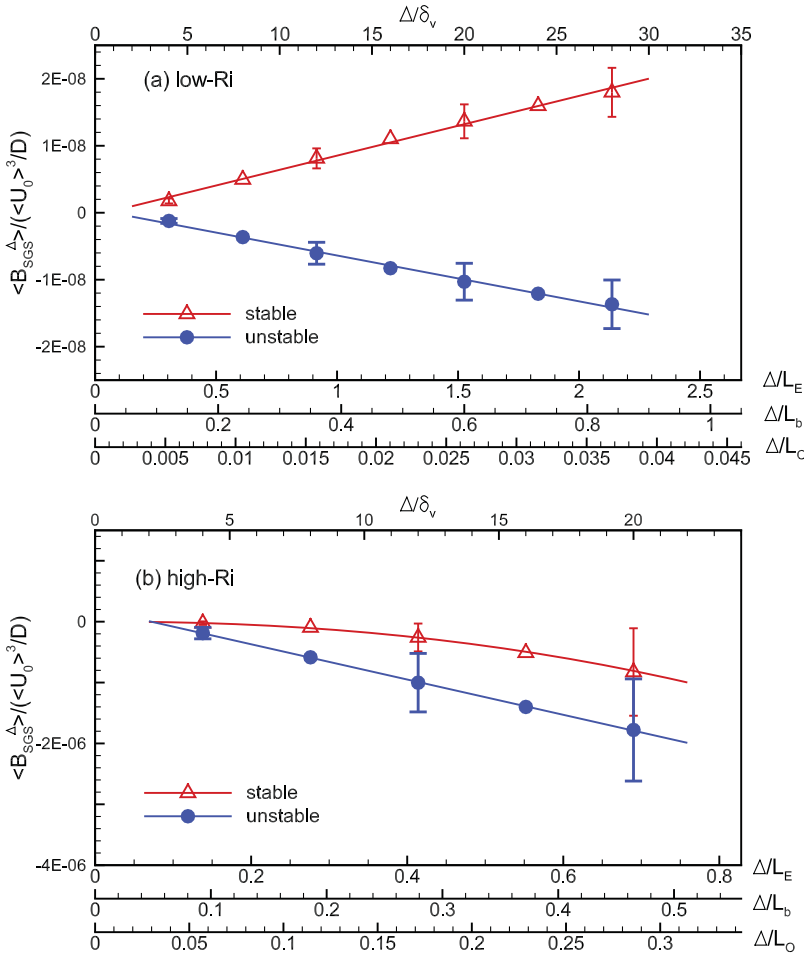
Figure 10. The spatially averaged mean of $\langle B_{SGS}^{\Delta} \rangle$ versus the filter scales in the stable and unstable stratification regions of the low-Ri case (top) and the high-Ri case (bottom). The error bars correspond to the standard deviations. The abscissas of Δ normalised by L_O, L_b and L_E are also shown.

stratification region experiences a destabilising process that breaks its flow structures. The gravitational instability and the Kelvin–Helmholtz instability are candidates of this destabilising mechanism.[50] In Figure 11, the positive $\langle B_{SGS}^{\Delta} \rangle$ (red) in the stable stratification region of the high-Ri case transits to negative values (light blue) in the shear layer as the jet develops to downstream, which suggests that the Kelvin–Helmholtz instability results in the destabilising process of flows in the stable stratification. The Kelvin–Helmholtz instability in the shear layer further contaminates the stable stratification region at even further downstream locations. Such an increasing contamination is also stimulated by the enhanced vertical kinetic energy, which is convected from the increased vertical kinetic energy originating from the gravitational instability in the unstable stratification region through the enhanced vorticity Ω_2. Different than the SGS production terms, in the stable stratification region, $\langle B_{SGS}^{\Delta} \rangle$ shows a weaker decreasing trend as Ri_b increases with an exception from the
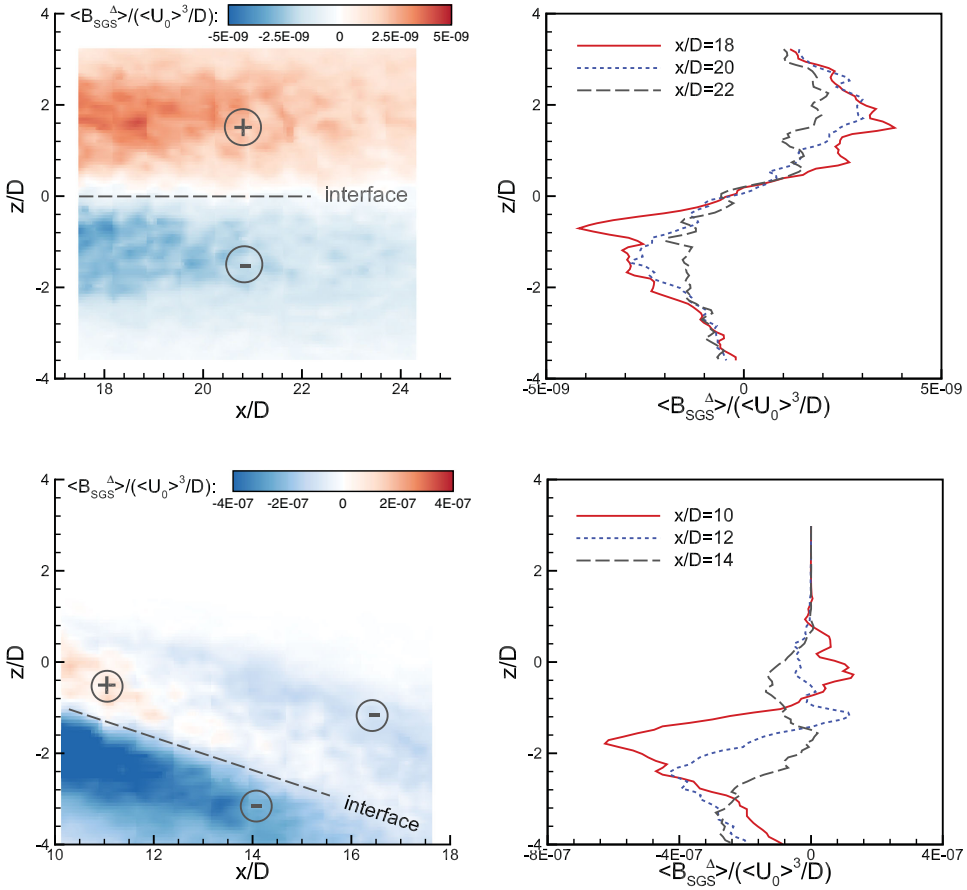
Figure 11. Contour (left) and profiles (right) of $\langle B_{SGS}^{\Delta}\rangle$ of the low-*Ri* case (top) and the high-*Ri* case (bottom). The data are from the scale $\Delta/\delta_v = 4$ for both cases. To be noted that the range of colour from the two contour plots are different.

unstable stratification region of the high-*Ri* case (as shown in Figure 12). In general, it implies that $\langle B_{SGS}^{\Delta}\rangle$ is contributed by both buoyancy and inertia effects (rather than a dominant one), which is the only channel that the buoyancy effect can influence the velocity field or communicate with the inertia effect.

It is challenging determining the viscous dissipation of SGS kinetic energy using the PIV data, since it requires all nine elements of S_{ij}. However, only four or five (if incompressibility holds) elements can be retrieved from two-dimensional PIV measurements. To compensate the estimation error due to the missing elements in S_{ij}, the local isotropy assumption introduced in [51] for RANS applications is adapted for LES in the present analysis, and the detailed derivation is given in Appendix 2. By assuming incompressible flow, the viscous dissipation of SGS kinetic energy can be estimated by

$$\langle \epsilon_{SGS}^{\Delta}\rangle \simeq 2\nu\langle 2(\widetilde{S_{11}S_{11}} - \widetilde{S}_{11}\widetilde{S}_{11}) + 2(\widetilde{S_{33}S_{33}} - \widetilde{S}_{33}\widetilde{S}_{33})$$
$$+ 2(\widetilde{S_{11}S_{33}} - \widetilde{S}_{11}\widetilde{S}_{33}) + 6(\widetilde{S_{13}S_{31}} - \widetilde{S}_{13}\widetilde{S}_{31})\rangle. \tag{13}$$
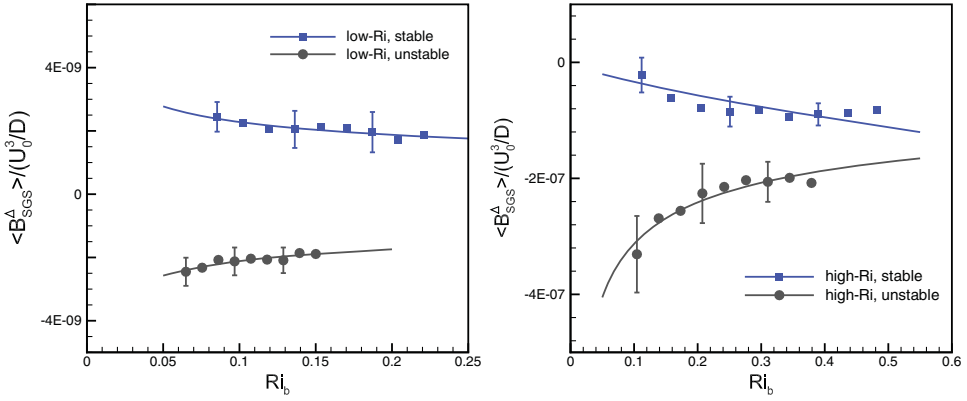
Figure 12. The dependence of $\langle B_{\text{SGS}}^{\Delta} \rangle$ on Ri_b in the stable and unstable stratification regions of the low-Ri case (left) and the high-Ri case (right). The curves are from power-law fitted data points. The error bars correspond to the standard deviations. Only $\Delta/\delta_v = 4$ data are shown for clarity.

The convection term in Equation (12) is also calculated by a surrogate, i.e.,

$$\left\langle \tilde{u}_j \frac{\partial k_{\text{SGS}}}{\partial x_j} \right\rangle \simeq \left\langle \tilde{u}_1 \frac{\partial k_{\text{SGS}}}{\partial x_1} \right\rangle + \left\langle \tilde{u}_3 \frac{\partial k_{\text{SGS}}}{\partial x_3} \right\rangle. \tag{14}$$

The turbulent transportation term cannot be directly measured in the experiments but can be evaluated through

$$\frac{\partial \langle T_i \rangle}{\partial x_i} \simeq \langle \Pi^{\Delta} \rangle - \left\langle B_{\text{SGS}}^{\Delta} \right\rangle - \left\langle \epsilon_{\text{SGS}}^{\Delta} \right\rangle - \left\langle \tilde{u}_j \frac{\partial k_{\text{SGS}}}{\partial x_j} \right\rangle. \tag{15}$$

In Figure 13, $\langle \epsilon_{\text{SGS}}^{\Delta} \rangle$ increases to approach constants as Δ increases to reach the inertial subrange for both cases. Additionally, in the low-Ri case, $\langle \epsilon_{\text{SGS}}^{\Delta} \rangle$ from the stable stratification region nearly overlaps with that from the unstable stratification region, in which the streamwise momentum is more dominant than the buoyancy effect so the results from both stratification regions are nearly identical. In the high-Ri case, $\langle \epsilon_{\text{SGS}}^{\Delta} \rangle$ from the unstable stratification region is apparently larger than that from the stable stratification region at all investigated filter scales, and the difference of $\langle \epsilon_{\text{SGS}}^{\Delta} \rangle$ between the stable and unstable stratification is due to the enhanced or damped mixing behaviour caused by the different roles of buoyancy effect in the two stratification regions. In the two study cases, the negative convection term $\langle \tilde{u}_j \partial k_{\text{SGS}} / \partial x_j \rangle$ acts as a source to the SGS kinetic energy, which, in general, is convected from the nearby upper stream locations and core of the jet. Meanwhile, $\partial \langle T_i \rangle / \partial x_i$ is a sink of SGS kinetic energy to diffuse the local SGS kinetic energy to the neighbouring locations. More importantly, the non-trivial $\langle \tilde{u}_j \partial k_{\text{SGS}} / \partial x_j \rangle$ and $\partial \langle T_i \rangle / \partial x_i$ make them non-neglectable, which makes the SGS energy balance $\langle \Pi^{\Delta} \rangle = \langle B_{\text{SGS}}^{\Delta} \rangle + \langle \epsilon_{\text{SGS}}^{\Delta} \rangle$, as examined in [28], invalid in this study. The discussions and calculation of energetic terms may be impacted by the errors of the surrogate, including the neglected term (e.g., $\langle \tau_{22} \widetilde{S}_{22} \rangle$ in $\langle \Pi^{\Delta} \rangle$) from measurements along the x_2 direction, the accuracy of modelling of the missing elements (e.g., local isotropic assumption in $\langle \epsilon^{\Delta} \rangle$, the discrete derivative accuracy especially when $\delta_v \gg \eta_k$ and $\delta_\theta \gg \eta_b$, etc.). However, the comparison and analysis between two
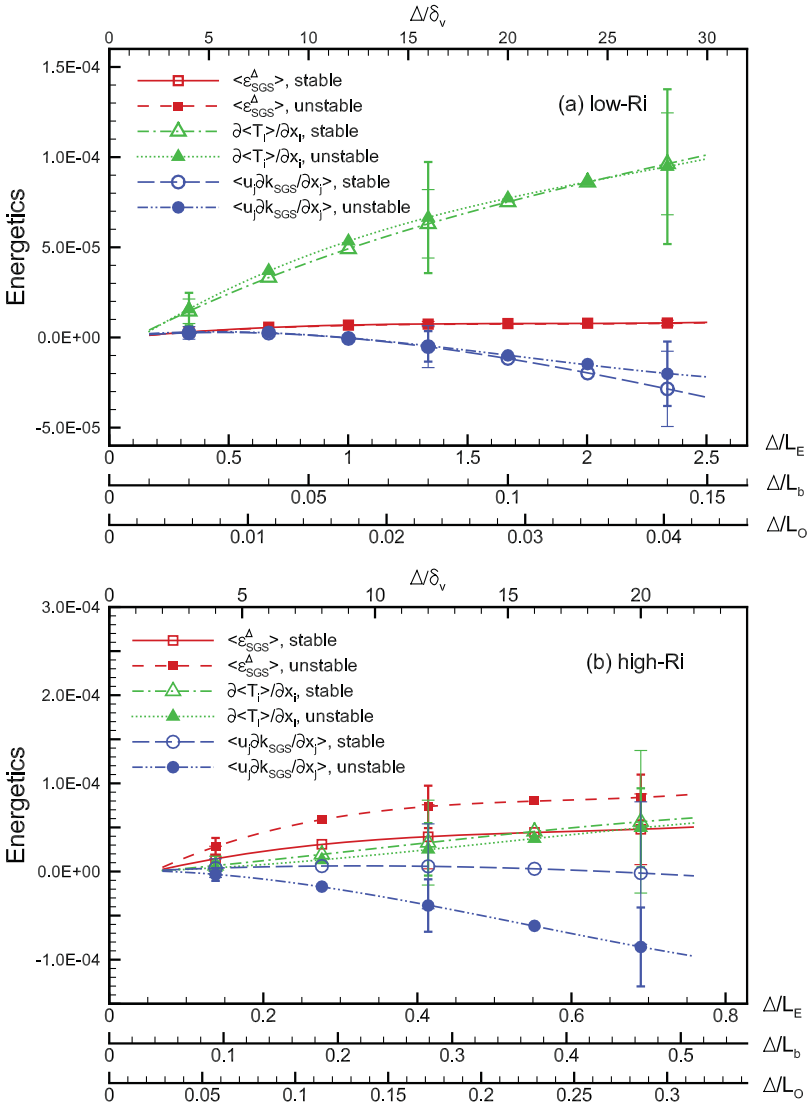
Figure 13. The spatially averaged mean of (non-dimensional) $\langle \epsilon_{SGS}^{\Delta} \rangle$, $\partial \langle T_i \rangle / \partial x_i$ and $\langle \tilde{u}_j \partial k_{SGS} / \partial x_j \rangle$ versus the filter scales in the stable and unstable stratification regions of the low-*Ri* case (top) and the high-*Ri* case (bottom). The error bars represent the standard deviations of the corresponding quantities. The abscissas of Δ normalised by L_O, L_b and L_E are shown, respectively.

stratification regions as well as two cases provide useful insights into the understanding of the role of SGS energetics. $\langle \epsilon_{SGS}^{\Delta} \rangle$ shows a decreasing trend as Ri_b increases (as shown in Figure 14), which demonstrates the inertia effect is more important in cascading the SGS kinetic energy to the smaller length scales.

3.3. Scale-invariance or scale-dependence of SGS model coefficients

One key requirement to LES SGS models is able to correctly predict the energetics of the resolved flow. Therefore, rather than retrieving the SGS model coefficients directly from
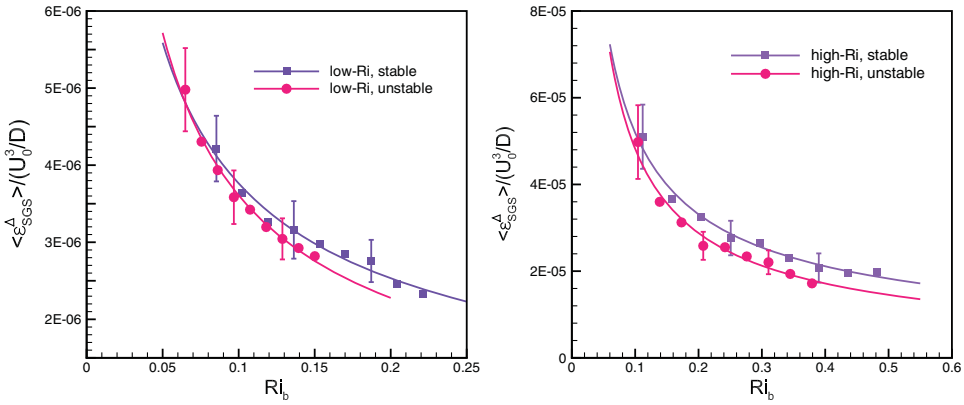
Figure 14. The dependence $\langle \epsilon_{SGS}^{\Delta} \rangle$ on Ri_b in the stable and unstable stratification regions of the low-*Ri* case (left) and the high-*Ri* case (right). The curves are plotted using the power-law fitted data points. The error bars correspond to the standard deviations. Only $\Delta/\delta_v = 4$ data are shown for clarity.

τ_{ij}^{Δ} and q_j^{Δ}, the model coefficients at a filter scale Δ can be obtained by matching the mean rate of production of SGS kinetic energy (as well as the rate of production of SGS scalar variance),[27] i.e.,

$$C_s^{2,\Delta} = \frac{-\langle \tau_{ij}^{\Delta} \widetilde{S}_{ij} \rangle}{\langle 2\Delta^2 |\widetilde{S}| \widetilde{S}_{ij} \widetilde{S}_{ij} \rangle}, \tag{16}$$

where $C_s^{2,\Delta}$ represents the determined value of C_s^2 at a filtering scale Δ. Similarly, Pr_{SGS}^{Δ} is determined from ν_{SGS} and κ_{SGS} by matching the mean rate of production of SGS scalar variance:

$$Pr_{SGS}^{-1,\Delta} \cdot C_s^{2,\Delta} = \frac{-\langle q_j^{\Delta} (\partial \widetilde{\theta}/\partial x_j) \rangle}{\langle \Delta^2 |\widetilde{S}| (\partial \widetilde{\theta}/\partial x_j)(\partial \widetilde{\theta}/\partial x_j) \rangle}, \tag{17}$$

i.e.,

$$Pr_{SGS}^{\Delta} = -C_s^{2,\Delta} \frac{\langle \Delta^2 |\widetilde{S}| (\partial \widetilde{\theta}/\partial x_j)(\partial \widetilde{\theta}/\partial x_j) \rangle}{\langle q_j^{\Delta} (\partial \widetilde{\theta}/\partial x_j) \rangle}. \tag{18}$$

To yield accurate predictions of energetics in stratified flows by using the Smagorinsky models, Pr_{SGS}^{Δ} and $C_s^{2,\Delta}$ (either *a-priori* prescribed or dynamically determined) should ideally be equal to the values determined by Equations (16) and (18). $C_s^{2,\Delta}$ determined by the scale-invariant dynamic Smagorinsky model (denoted by a subscript SID) is computed by first applying a test-filter operation at the scale $\alpha\Delta$ and denoted by $\overline{(\cdot)}$

$$C_s^{2,\Delta}|_{SID} = \frac{\langle L_{ij} M_{ij} \rangle}{\langle M_{ij} M_{ij} \rangle}, \tag{19}$$

where $L_{ij} = \overline{\widetilde{u_i}\widetilde{u_j}} - \widetilde{\overline{u}_i\overline{u}_j}$, $M_{ij} = 2\Delta^2 (\overline{|\widetilde{S}|\widetilde{S}_{ij}} - \alpha^2 |\widetilde{\overline{S}}|\widetilde{\overline{S}}_{ij})$ and $\langle \cdot \rangle$ is an averaging operation to minimise the error of the Germano identity.[27] Similarly,

$$Pr^{\Delta}_{\text{SGS}}|_{\text{SID}} = C_s^{2,\Delta}|_{\text{SID}} \cdot \frac{\langle X_j X_j \rangle}{\langle K_j X_j \rangle}, \tag{20}$$

where $K_j = \overline{\widetilde{u}_j\widetilde{\theta}} - \widetilde{\overline{u}_j\overline{\theta}}$ and $X_j = \alpha^2 \left(\overline{|\widetilde{S}|\partial\widetilde{\theta}/\partial x_j} - \alpha^2 |\widetilde{\overline{S}}|\partial\widetilde{\overline{\theta}}/\partial x_j \right)$. The key assumption behind this scale-invariant dynamic model is the scale-invariance of $C_s^{2,\Delta}$, i.e.,

$$C_s^{2,\alpha\Delta}|_{\text{SID}} = C_s^{2,\Delta}|_{\text{SID}}. \tag{21}$$

The same treatment can be applied to Pr^{Δ}_{SGS}. To relax this scale-invariant assumption, the scale-dependent dynamic Smagorinsky model (denoted as SDD) introduces a second test filtering operation at length scale $\alpha^2 \Delta$ [22,23] by assuming a power function, i.e.,

$$C_s^{2,\Delta}|_{\text{SDD}} \propto \Delta^{\phi} \quad \text{or equivalently} \quad C_s^{2,\alpha\Delta}|_{\text{SDD}} = C_s^{2,\Delta}|_{\text{SDD}} \cdot \alpha^{\phi}, \tag{22}$$

where ϕ is a dynamically determined power coefficient. This scale-dependent dynamic assumption was tested using the field measurement data from 16 anemometers in ABL.[34] However, different small scale turbulence can be represented by different superstatistics models,[52] thus the potential difference of turbulence in ABL and other flows (e.g., lab experiments) stimulates a rational question about the validity of this assumed scale-invariance or scale-dependence. To address this question, we examine the PDFs of $C_s^{2,\Delta}$ and $C_s^{2,\Delta}/Pr^{\Delta}_{\text{SGS}}$, respectively, against the filter scales, as shown in Figure 15. The dashed lines indicate the standard Smagorinsky SGS model coefficient $C_s = 0.17$ and $Pr_{\text{SGS}} = 0.7$ as commonly used in numerical simulations. With the same amount of data, the results from the low-Ri case shows relatively converged distributions of $C_s^{2,\Delta}$ and $C_s^{2,\Delta}/Pr^{\Delta}_{\text{SGS}}$ at all studied Δ's. In the low-Ri case, the maximum likelihood of $C_s^{2,\Delta}$ occurs around a nearly constant value ($C_s^2 \simeq 0.014$ or $C_s \simeq 0.12$); the peak of PDF for $C_s^{2,\Delta}/Pr^{\Delta}_{\text{SGS}}$ at different scales varies in a wide range, while the maximum of these peaks occurs at $\Delta \simeq 5\delta_v$. The value of $C_s = 0.17$ from a theoretical derivation [19] is distinctly larger than the value determined by the present experimental results ($C_s \simeq 0.12$), although a constant C_s^2 cannot fully predict the scale dependence. In addition, the large variations of $C_s^{2,\Delta}/Pr^{\Delta}_{\text{SGS}}$ imply the small-scale turbulence triggered by the scalar fields is not 'equivalent' to that of velocity fields, which further emphasises the necessity of investigating both fields at the same time, as well as interactions between the small-scale quantities between the velocity and scalar fields. For the high-Ri case, the needed values of $C_s^{2,\Delta}$ spread widely at a scale when $\Delta < 10\delta_v$ and its distribution disperses into three branches when $\Delta > 10\delta_v$. $C_s^{2,\Delta}/Pr^{\Delta}_{\text{SGS}}$ shows a weak branch-like distribution, whose branch-like trend is not as strong as that in the low-Ri case. Its mean value is less than that of the low-Ri case. It is interesting to observe the branch-like distribution of $C_s^{2,\Delta}$. Equation (16) suggests that $C_s^{2,\Delta}$ represents the ratio of the energy transferred to SGS to the resolved kinetic energy at a filter scale Δ. In the high-Ri case, $\langle B^{\Delta}_{\text{SGS}} \rangle$ influences the vertical momentum in the stable stratification region to cause an anisotropic turbulence with a x_1-preference but with a x_3-preference in the unstable stratification region. As a result, $C_s^{2,\Delta}$ stimulates a more efficient convert of the resolved
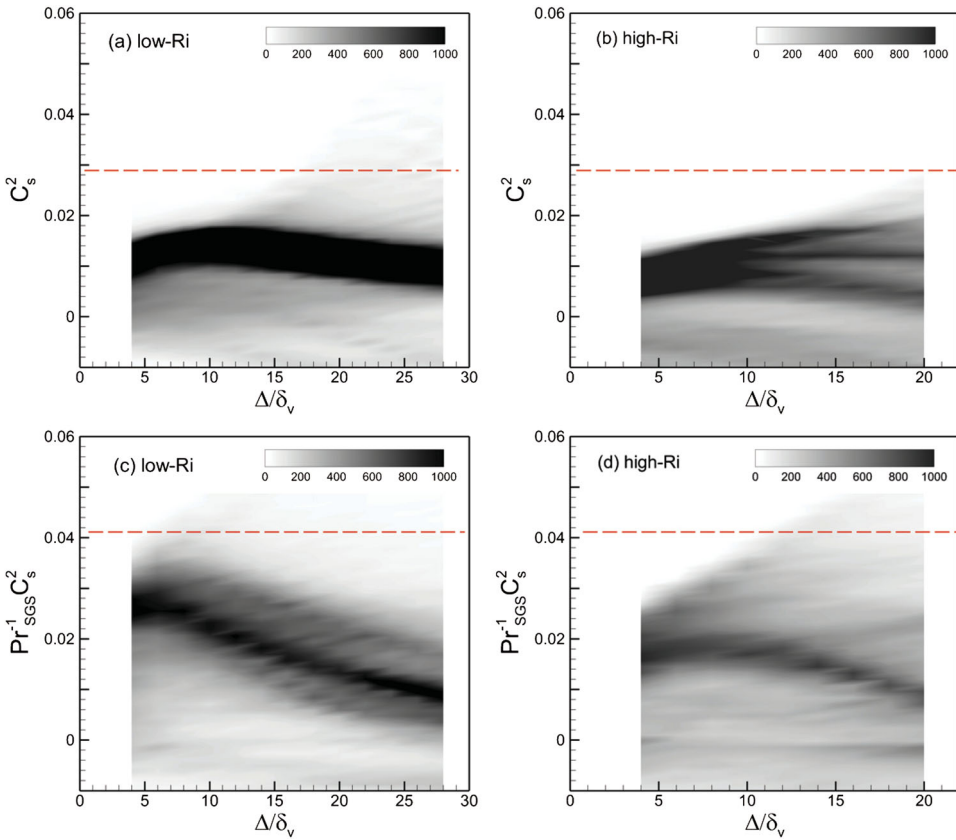
Figure 15. PDF of $C_s^{2,\Delta}$ (a, b) and $C_s^{2,\Delta}/Pr_{SGS}^{\Delta}$ (c, d) against Δ's. The dashed lines indicate the standard Smagorinsky subgrid-scale model coefficients ($C_s = 0.17$ and $Pr_{SGS} = 0.7$) as commonly used. Legends represent the relative values of the PDFs.

kinetic energy to span a wider range of length scales (as implied in Figure 7) in the stable stratification region than that in the unstable one. With plotting the data within the single stratification region (identified by Ri_g), the three branches (from top to bottom) in Figure 15(b) and 15(d) are identified to correspond to the data from the stable stratification region, the interim region and the unstable stratification region, respectively. The branch-like distribution, therefore, originates from the different characteristic local length scales of the dissipating path of eddies within the inertial range due to different stratification, and the vanishing branch-like distribution beyond the inertial range suggests a potential universality with independence of stratification. The length scale connecting the inertial and the dissipation range is the approximate start of the universality regime.

Using the same data-set, the conditional average of $C_s^{2,\alpha\Delta}/C_s^{2,\Delta}$ upon α is calculated to examine the scale-dependence of $C_s^{2,\Delta}$. Here, the data are used as a whole piece rather than distinguished by separated stable and unstable stratification regions, since the practical LES domain cannot be predetermined into different regions. Dynamic SGS models rely on the assumption that the numerical grid sizes (the smallest resolved scales) fall into the inertial subrange everywhere in the modelling domain. Therefore, first, we choose the $C_s^{2,\Delta/\delta_v=8}$ (with the filter scale locating in the inertial range) as a reference. Figure 16 shows the power
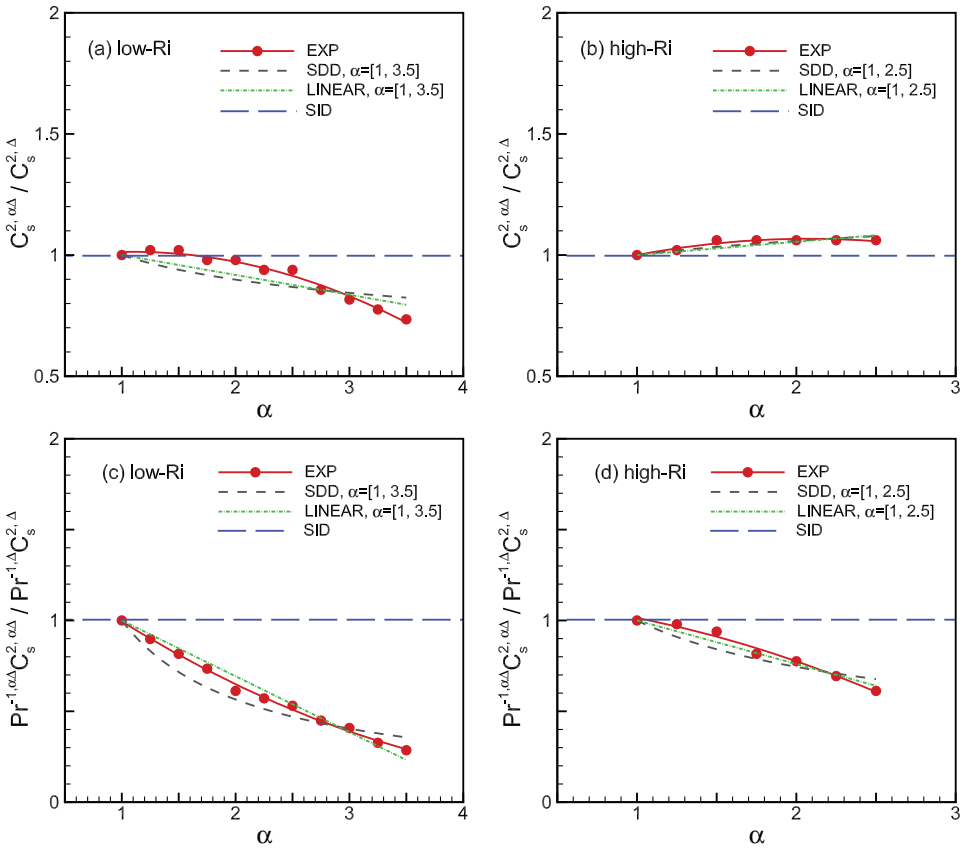
Figure 16. The conditional averages of $C_s^{2,\alpha\Delta}/C_s^{2,\Delta}$ and $(Pr_{SGS}^{-1,\alpha\Delta}C_s^{2,\alpha\Delta})/(Pr_{SGS}^{-1,\Delta}C_s^{2,\Delta})$ with a reference of data at $\Delta/\delta_v = 8$. The blue dashed lines indicate the scale-invariant assumption; the grey dashed lines represent the power-law scale-dependence; the green dashed–dotted lines show linear scale-dependence; the red solid lines are second-polynomial curve fits of the experimental data marked by red circles.

law assumption in scale-dependent dynamic models (grey lines) can successfully capture the variation of $C_s^{2,\alpha\Delta}/C_s^{2,\Delta}$ [or $(Pr_{SGS}^{-1,\alpha\Delta}C_s^{2,\alpha\Delta})/(Pr_{SGS}^{-1,\Delta}C_s^{2,\Delta})$]. However, a linear function through (1, 1), such as $C_s^{2,\alpha\Delta}/C_s^{2,\Delta} = c \cdot \alpha + 1 - c$ (green lines), can present the trend but with smaller fitness errors, where c as a coefficient can be obtained through two filtering operations at scales of $\alpha\Delta$ and $\alpha^2\Delta$.

The intermittent nature of turbulence makes the local characteristic length scales of flows vary temporally, which causes the gaps between the local integral length scale and the local Kolmogorov length scale to vary in the flow field. In some portion of the simulation domain, the grid sizes ($\Delta's$) therefore do not always locate within the inertial subrange, i.e., sometimes close to or within the energy-containing range and sometimes in the dissipation range. If the numerical grid sizes approach to the local integral length scales, LES will fail to accurately predict the unsteady flows, which relies more on the accuracy of SGS models. On the other side, if the numerical grid sizes fall into the local dissipation range, what is the performance of SGS models? Is there any restriction on choosing α? To address these questions, $C_s^{2,\Delta/\delta_v=4}$ (with the filter scale locating in the dissipation range) is
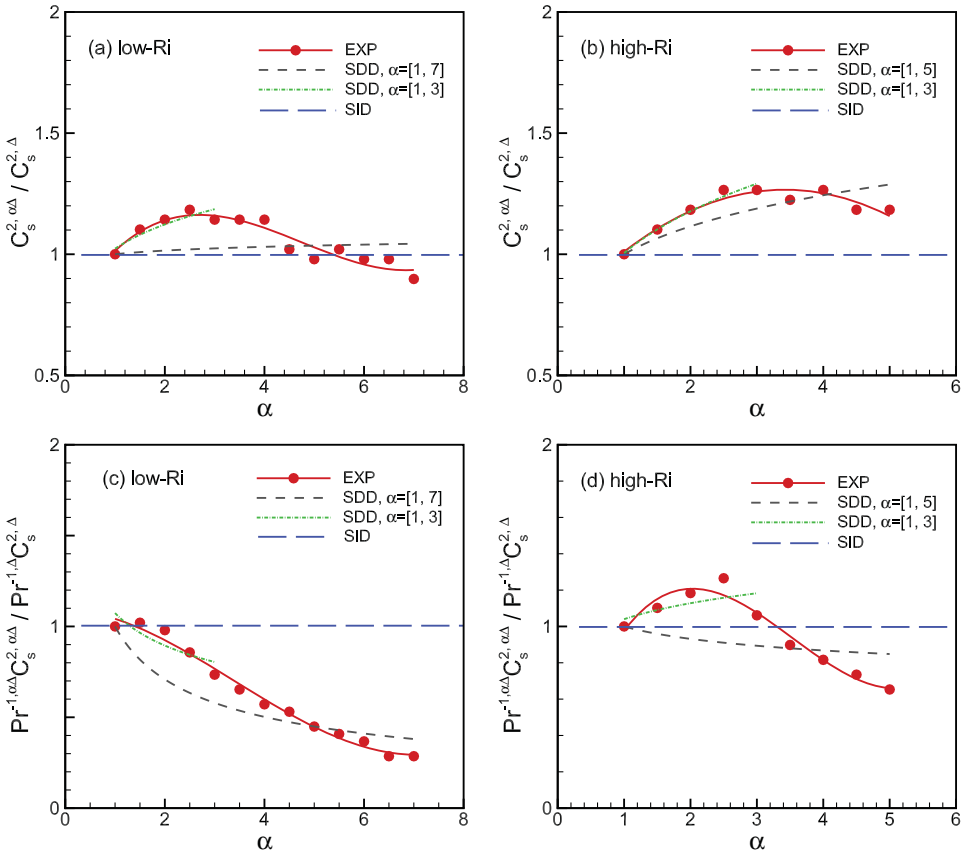
Figure 17. The conditional averages of $C_s^{2,\alpha\Delta}/C_s^{2,\Delta}$ and $(Pr_{SGS}^{-1,\alpha\Delta}C_s^{2,\alpha\Delta})/(Pr_{SGS}^{-1,\Delta}C_s^{2,\Delta})$ with a reference of data at $\Delta/\delta_v = 4$. The blue dashed lines indicate the scale-invariant assumption; the grey solid lines represent power-law scale-dependence fitted using α of all scales; the green solid lines are fitted using data in $1 \le \alpha \le 3$; the red solid lines are from third-order polynomial curve fit of the experimental data marked by red circles.

selected as a reference to examine the basic assumptions of SGS models again (as shown in Figure 17). For the low-Ri and high-Ri cases, $C_s^{2,\alpha\Delta}/C_s^{2,\Delta}$ varies from 0.9 to 1.3 while $(Pr_{SGS}^{-1,\alpha\Delta}C_s^{2,\alpha\Delta})/(Pr_{SGS}^{-1,\Delta}C_s^{2,\Delta})$ ranges between 0.4 and 1.3 over the tested α's. The power-law scale-dependence, i.e., $C_s^{2,\alpha\Delta}/C_s^{2,\Delta} \sim \alpha^\phi$, is approximately able to describe the trend for $C_s^{2,\alpha\Delta}/C_s^{2,\Delta}$ if a narrow band of α (e.g., $1 \le \alpha \le 3$) are used. However, if data fitted with a wider range of α (e.g., $1 \le \alpha \le 7$ for the low-Ri case or $1 \le \alpha \le 5$ for the high-Ri case) false predictions are observed, which in other words suggests erroneous modellings of $C_s^{2,\Delta}$ and Pr_{SGS}^Δ. This error, however, cannot be retrieved if a narrow range of α, e.g., $\alpha \le 3$ (or even smaller value $\alpha = 1.75$ [34]) is examined. It elucidates that the performance of the dynamic SGS models is sensitive to the chosen α, and $1 < \alpha \le 3$ is suggested to be capable of providing reasonable simulation results. Former studies focus on the influence of local stability parameters on $C_s^{2,\Delta}$ and Pr_{SGS}^Δ.[53] The narrow range of length scales in the laboratory experiments is not ideal to study this influence. The local stratification Ri_b is found to have strong influence to the SGS energetic terms, but Pr_{SGS}^Δ and $C_s^{2,\Delta}$ do not depend on Ri_b (results not shown here).

4. Conclusion

In this study, a high-resolution experimental data-set of velocity-scalar field is applied to study the SGS physics in a stratified jet with coexistence of stable and unstable stratification by examining key parameters including the production of SGS kinetic energy $\langle \Pi^\Delta \rangle$, the production of SGS scalar variance $\langle \chi^\Delta \rangle$, and the SGS buoyant destruction $\langle B_{SGS}^\Delta \rangle$. The SGS models are also examined by *a-priori* tests[2]. The main findings are summarised as following.

(1) In the low-*Ri* case, $\langle \Pi^\Delta \rangle$ (or $\langle \chi^\Delta \rangle$) presents a similar distribution against the filter scale Δ's in both stable and unstable stratification regions. As Δ increases within the dissipation range, $\langle \Pi^\Delta \rangle$ (or $\langle \chi^\Delta \rangle$) increases, and they approach a plateau when Δ's locate in the inertial subrange (see Figure 8), which demonstrates the conserved energy decay rate in its cascade process. In the high-*Ri* case, $\langle \Pi^\Delta \rangle$ (or $\langle \chi^\Delta \rangle$) shows significant difference between the stable and unstable stratification regions. In the stable stratification region, $\langle \Pi^\Delta \rangle$ (or $\langle \chi^\Delta \rangle$) is larger than that in the unstable stratification region, and it increases with Δ. However, in the unstable stratification region, $\langle \Pi^\Delta \rangle$ (or $\langle \chi^\Delta \rangle$) increases to reach a plateau and follows a decrease. Such a difference is a sign of the different role of $\langle B_{SGS}^\Delta \rangle$ in the two stratification regions.

(2) $\langle B_{SGS}^\Delta \rangle$ serves a role of turbulence damping in the stable stratification to assist the viscous dissipation to balance the production of turbulence. On the other hand, it behaves like an additional turbulence generation mechanism (as shown in Figure 10). This is true in the low-*Ri* case but fails in the stable stratification of high-*Ri* case where $\langle B_{SGS}^\Delta \rangle$ turns to be a source of SGS kinetic energy to make the local stable stratification destabilised. The candidate mechanism behind this is possibly the coupled mechanism of KH instability in the 'semi-stable' stratification and the gravitational instability in the unstable stratification region.

(3) The examination of SGS energetics identifies the role of each term in Equation (12). The non-trivial contributions of $\partial \langle T_i \rangle / \partial x_i$ and $\langle \tilde{u}_j \partial k_{SGS} / \partial x_j \rangle$ do not support the energy balance assumption $\langle \Pi^\Delta \rangle = \langle B_{SGS}^\Delta \rangle + \langle \epsilon_{SGS}^\Delta \rangle$, which stands in the ABL study.[28] The failure may be caused by the fact that the transportation of kinetic energy is stronger in the jet than that in ABL, to contribute to a non-trivial convection and transportation term.

(4) In the examination of SGS models, the scale-invariant dynamic model and the standard Smagorinksy model present unsatisfactory predictions while the scale-dependent assumption is more realistic. However, the scale-dependent dynamic models are sensitive to the assumption that filtering scales in the inertial subrange, which is not satisfied everywhere in the simulations. When the filter scales locates in the inertial subrange, $C_s^{2,\alpha\Delta}/C_s^{2,\Delta} = \Delta^\phi$ is valid. If the filter scale locates in the dissipation range, the scale-dependent dynamic model presents an error trend of $C_s^{2,\alpha\Delta}/C_s^{2,\Delta}$ when a wider range of α (e.g., $1 \le \alpha \le 7$ for the low-*Ri* case) is applied, and similar discoveries are also found in the scalar field (e.g., $Pr_{SGS}^{-1,\Delta} C_s^{2,\Delta}$). The incorrect representation of such a trend is however difficult to be revealed if a narrower range of α, e.g., $\alpha \le 3$ in this study (green lines in Figure 17). The chosen value of α significantly influences the performance of scale-dependent dynamic model in such flow conditions. The examinations give a upper limit of α (≤ 3) to satisfy the dynamic scale-dependent assumptions with a balance consideration.

The simultaneous velocity-scalar measurements in this study present an effective platform to investigate the SGS stratified turbulence. However, two-dimensional data need certain assumptions (like the symmetry assumption in this study) for analysis and using surrogates which brings in discrepancies for highly three-dimensional turbulence. To conquer such limits, time-resolved three-dimensional data-sets are necessarily required for more insights into the concomitantly stably and unstably stratified turbulence as well as to improve SGS models for LES.

Notes

1. The eddy diffusivity of heat and eddy diffusivity of density are equal when density variations are dominated by those of temperatures, as in many applications of stratified flows. Details can be found, e.g., in [3] (page 42). Thus, here we do not differentiate them, as well as turbulent Prandtl number and turbulent Schmidt number.
2. The *a-posteriori* examinations of the same problem can be found in [54].

Acknowledgements

Disclosure statement

No potential conflict of interest was reported by the authors.

References

[1] Turner JS. Buoyancy effects in fluids. Cambridge (UK): Cambridge University Press; 1973.
[2] Simpson J. Gravity currents: in the environment and the laboratory. 2nd ed. Cambridge (UK): Cambridge University Press; 1997.
[3] Thorpe SA. An introduction to ocean turbulence. Cambridge (NY): Cambridge University Press; 2007.
[4] De Silva I, Fernando H, Eaton F. Evolution of Kelvin-Helmholtz billows in nature and laboratory. Earth Planet Sc Lett. 1996;143:217–231.
[5] Riley J, Lelong MP. Fluid motions in the presence of strong stratification. Ann Rev Fluid Mech. 2000;32:613–657.
[6] Lumley JL. Computational modeling of turbulent flows. Adv Appl Mech. 1978;18:123–176.
[7] Cheng Y, Howard A. An improved model for the turbulent PBL. J Atmos Sci. 2002;59:1550–1565.
[8] Tseng YH, Dietrich DE. Entrainment and transport in the three-dimensional idealized gravity current simulation. J Atmos Sci. 2006;23:613–657.
[9] Ilicak M, Özgökmen TM, Baumert HZ, et al. Performance of two-equation turbulence closures in three-dimensional simulations of the Red Sea overflow. Ocean Model. 2008;24:122–139.
[10] Özgökmen T, Iliescu T, Fischer P. Large eddy simulation of stratified mixing in a three-dimensional lock-exchange system. Ocean Model. 2009;26:134–155.
[11] Gayen B, Sarkar S, Taylor JR. Large eddy simulation of a stratified boundary layer under an oscillatory current. J Fluid Mech. 2010;643:233–266.
[12] Ooi SK, Constantinescu G, Weber LJ. Numerical simulations of lock exchange compositional gravity currents. J Fluid Mech. 2009;635:361–388.
[13] Moeng CH, McWilliams JC, Rotunno R, et al. Investigating 2D modelling of atmospheric convection in the PBL. J Atmos Sci. 2003;61:889–903.
[14] Weil JC, Sullivan PP, Moeng CH. The use of large-eddy simulations in Lagrangian particle dispersion models. J Atmos Sci. 2004;61:2877–2887.

[15] Beare R, Macvean MK, Holtslag AAM, et al. An intercomparison of large-eddy simulations of the stable boundary layer. Bound.-Lay. Meteorol. 2006;118:247–272.

[16] Kumar V, Svensson G, Holtslag A, et al. Impact of surface flux formulations and geostrophic forcing on large-eddy simulations of diurnal atmospheric boundary layer flow. J Appl Meteor Climatol. 2010;49:1496–1516.

[17] Sagaut P. Large eddy simulation for incompressible flows. 3rd ed. Berlin: Springer; 2006.

[18] Smagorinsky J. General circulation experiments with the primitive equations. I. The basic experiment. Mon Weather Rev. 1963;91:99–164.

[19] Lilly DK. The representation of small-scale turbulence in numerical simulation experiments. In: Goldstine HH, editor. Proceedings of the IBM Scientific Computing Symposium on Environmental Sciences. Yorktown Heights, NY: IBM; 1967. p. 195–210.

[20] Sullivan PP, Horst TW, Lenschow DH, et al. Structure of subfilter-scale fluxes in the atmospheric surface layer with application to large-eddy simulation modelling. J Fluid Mech. 2003;482:101–139.

[21] Germano M, Piomelli U, Moin P, et al. A dynamic subgrid-scale eddy viscosity model. Phys. Fluids. 1991;3:1760–1765.

[22] Porté-Agel F, Meneveau C, Parlange MB. A scale-dependent dynamic model for large-eddy simulation: Application to a neutral atmoshperic boundary layer. J Fluid Mech. 2000;415:261–284.

[23] Porté-Agel F. A scale-dependent dynamic model for scalar transport in large-eddy simulation of the atmospheric boundary layer. Bound-Lay Meteorol. 2004;112:81–105.

[24] Zhou BW, Chow FK. Large-eddy simulation of the stable boundary layer with explicit filtering and reconstruction turbulence modeling. J Atmos Sci. 2011;68:2142–2155.

[25] Armenio V, Sarkar S. An investigation of stably stratified turbulent channel flow using large-eddy simulation. J Fluid Mech. 2002;459:1–42.

[26] Liu S, Meneveau C, Katz J. On the properties of similarity subgrid-scale models as deduced from measurements in a turbulent jet. J Fluid Mech. 1994;275:83–119.

[27] Meneveau C, Katz J. Scale invariance and turbulence models for large-eddy simulation. Ann Rev Fluid Mech. 2000;32:1–32.

[28] Bou-Zeid E, Higgins C, Huwald H, et al. Field study of the dynamics and modelling of subgrid-scale turbulence in a stable atmospheric surface layer over a glacier. J Fluid Mech. 2010;665:480–515.

[29] Pope S.B. Turbulent flows. Cambridge: Cambridge University Press; 2001.

[30] Molemaker M, McWilliams J, Capet X. Balanced and unbalanced routes to dissipation in an equilibrated Eady flow. J Fluid Mech. 2010;654:35–63.

[31] Lindborg E. The energy cascade in a strongly stratified fluid. J Fluid Mech. 2006;550:207–242.

[32] Bartello P, Tobias S. Sensitivity of stratified turbulence to the buoyancy Reynolds number. J Fluid Mech. 2013;725:1–22.

[33] Horst T, Kleissl J, Lenschow D, et al. HATS: field observations to obtain spatially filtered turbulence fields from crosswind arrays of sonic anemometers in the atmospheric surface layer. J Atmos Sci. 2004;61:1566–1581.

[34] Kleissl J, Parlange MB, Meneveau C. Field experimental study of dynamic Smagorinsky models in the atmospheric surface layer. J Atmos Sci. 2004;61:2296–2307.

[35] Feng H, Olsen MG, Hill JC, et al. Simultaneous velocity and concentration field measurements of passive-scalar mixing in a confined rectangular jet. Exp Fluids. 2007;42:847–862.

[36] Odier P, Chen J, Ecke R. Entrainment and mixing in a laboratory model of oceanic overflow. J Fluid Mech. 2014;746:498–535.

[37] Xu D, Chen J. Experimental study of stratified jet by simultaneous measurements of velocity and density fields. Exp Fluids. 2012;53:145–162.

[38] Chen J, Meneveau C, Katz J. Scale interactions of turbulence subjected to a straining-relaxation-destraining cycle. J Fluid Mech. 2006;562:123–150.

[39] Zhang J, Tao B, Katz J. Turbulent flow measurement in a square duct with hybrid holographic PIV. Exp Fluids. 1997;23:373–381.

[40] Gargett AE, Osborn TR, Nasmyth PW. Local isotropy and the decay of turbulence in a stratified fluid. J Fluid Mech. 1984;144:231–280.

[41] Brethouwer G, Billant P, Lindborg E, et al. Scaling analysis and simulation of strongly stratified turbulent flows. J Fluid Mech. 2007;585:343–368.

[42] Billant P, Chomaz J. Self-similarity of strongly stratified inviscid flows. Phys Fluids. 2001;13:1645–1651.

[43] Waite ML. Stratified turbulence at the buoyancy scale. Phys Fluids. 2011;23:066602.

[44] Baumert H, Peters H. Second-momentum closures and length scales for weakly stratified turbulent shear flows. J Geophys Res. 2000;105:6453–6468.

[45] Schumann U, Gerz T. Turbulent mixing in stably stratified shear flows. J Appl Meteorol. 1995;34:33–48.

[46] Rohr J. An experimental study of evolving turbulence in uniform mean shear flow with and without stable stratification [thesis]. San Diego (CA): University of California; 1985.

[47] Canuto VM, Howard A, Cheng Y, et al. Ocean turbulence. Part I: one-point closure model. Momentum and heat vertical diffusivities. J Phys Oceanogr. 2001;31:1413–1426.

[48] Kantha LH, Clayson CA. An improved mixed layer model for geophysical applications. J Geophys Res. 1994;99:235–266.

[49] Mellor GL, Yamada T. A hierarchy of turbulence closure models for planetary boundary layers. J Atmos Sci. 1974;31:1791–1806.

[50] McWilliams J, Molemaker M. Ageostrophic, anticyclonic instability of a geostrophic, barotropic boundary current. Phys Fluids. 2004;16:3720–3725.

[51] Doron P, Bertuccioli L, Katz J, et al. Turbulence characteristics and dissipation estimates in the coastal ocean bottom boundary layer from PIV data. J Phys Oceanogr. 2001;31:2108–2134.

[52] Beck C. Superstatistics in hydrodynamic turbulence. Physica D. 2004;193:195–207.

[53] Kleissl J, Meneveau C, Parlange MB. On the magnitude and variability of subgrid-scale eddy-diffusion coefficients in the atmospheric surface layer. J Atmos Sci. 2003;60:2372–2388.

[54] Ghaisas NS, Shetty DA, Frankel SH. Large eddy simulation of turbulent horizontal buoyant jets. J Turbul. 2015;16:772–808.

Appendices

Appendix 1. Quality of discrete derivatives

The five-point discrete derivative algorithm is validated by quantifying the error of calculating the divergence-free condition of the resolved velocity field ($\partial \tilde{u}_i / \partial x_i = 0$) as reported in [39]. A quality parameter is introduced:

$$Q = \frac{(\langle \partial \tilde{u}_1 / \partial x_1 \rangle + \langle \partial \tilde{u}_2 / \partial x_2 \rangle + \langle \partial \tilde{u}_3 / \partial x_3 \rangle)^2}{(\langle \partial \tilde{u}_1 / \partial x_1 \rangle)^2 + (\langle \partial \tilde{u}_2 / \partial x_2 \rangle)^2 + (\langle \partial \tilde{u}_3 / \partial x_3 \rangle)^2}. \tag{A1}$$

Most parameters investigated in this work, e.g., $\langle \Pi^{\Delta} \rangle$ or $\langle \chi^{\Delta} \rangle$, involve an ensemble average operation, thus Q is estimated using the averaged derivatives. One is reminded that $\partial \tilde{u}_2 / \partial x_2$ cannot be obtained due to the two-dimensional nature of the measurement techniques. However, with the assumption of $\partial \langle \tilde{u}_2 \rangle / \partial x_2 = 0$ based on the symmetry with respect to the central $x_1 - x_3$ plane ($x_2 = 0$), the calculation of quality Q can be analysed using the measured velocity u_1 and u_3. If the discrete derivative approach produces an accurate estimate, $Q \simeq 0$, but if the derivative approach is not able to present a good estimate, Q approaches 2 (it is 3 if using three velocity components) when the two velocity derivatives are equal. The parameter Q is calculated using the experimental data of the low-Ri and high-Ri cases at different filtering scales and the probability density function of Q is shown in Figure A1. The median of Q is about 0.28 and its mean is about 0.47 for the low-Ri case, while the median and mean of Q are about 0.08 and 0.31 respectively for the high-Ri case. These values are lower than the median of 0.29 and the mean of 0.6 reported in [28] (where 3
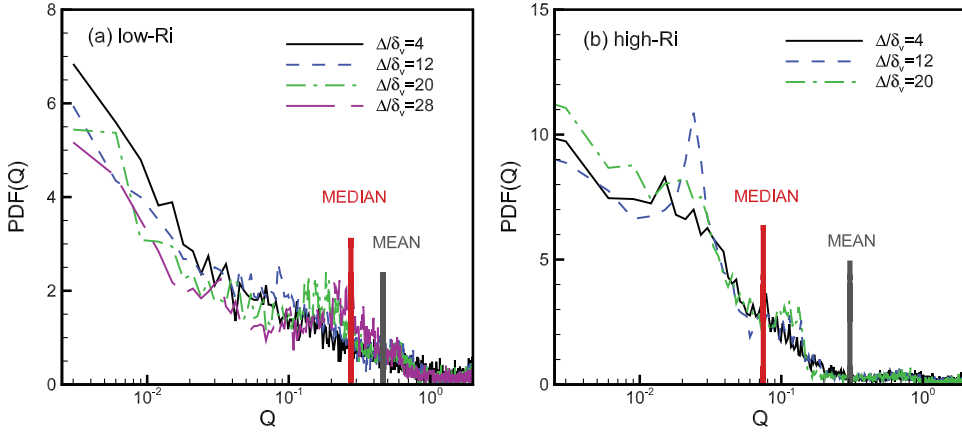
Figure A1. Probability density function of the quality parameter Q for (a) the low-*Ri* case and (b) the high-*Ri* case at different filtering scales. Only results from selected Δ's are shown here for clarity of display. Note that precise measurements and accurate discrete derivative calculations should give $Q \simeq 0$.

velocity components used), as well as much lower than the median of 1.18 and the mean of 1.27 when the data are normally distributed (with the mean of zero). More importantly, 65% data points have $Q < 0.47$ for the low-*Ri* case and 73% data points have $Q < 0.31$ for the high-*Ri* case. The good results of Q on the other side illustrate the validation of assumption of $\partial \langle \tilde{u}_2 \rangle / \partial x_2 \simeq 0$.

Appendix 2. Adaptation of local isotropy assumption for LES

From planar PIV measurement results, to calculate the viscous dissipation of turbulent kinetic energy under Reynolds decomposition, a local isotropy assumption was introduced to compensate the missing terms of fluctuating strain rate $s'_{ij} = 0.5(\partial u'_i/\partial x_j + \partial u'_j/\partial x_i)$, where $u'_i = u_i - \langle u_i \rangle$ is the fluctuation part of velocity. The detailed derivation of this assumption is given in [51]. By analogy, the following derivation is the adaption of this assumption for LES, i.e.,

$$\left\langle \widetilde{\left(\frac{\partial u_1}{\partial x_2}\right)^2} - \left(\widetilde{\frac{\partial u_1}{\partial x_2}}\right)^2 \right\rangle \simeq \left\langle \widetilde{\left(\frac{\partial u_2}{\partial x_1}\right)^2} - \left(\widetilde{\frac{\partial u_2}{\partial x_1}}\right)^2 \right\rangle \simeq \left\langle \widetilde{\left(\frac{\partial u_2}{\partial x_3}\right)^2} - \left(\widetilde{\frac{\partial u_2}{\partial x_3}}\right)^2 \right\rangle$$

$$\simeq \left\langle \widetilde{\left(\frac{\partial u_3}{\partial x_2}\right)^2} - \left(\widetilde{\frac{\partial u_3}{\partial x_2}}\right)^2 \right\rangle \simeq \frac{1}{2} \left\langle \widetilde{\left(\frac{\partial u_1}{\partial x_3}\right)^2} - \left(\widetilde{\frac{\partial u_1}{\partial x_3}}\right)^2 + \widetilde{\left(\frac{\partial u_3}{\partial x_1}\right)^2} - \left(\widetilde{\frac{\partial u_3}{\partial x_1}}\right)^2 \right\rangle \quad \text{(B1)}$$

and

$$\left\langle \widetilde{\left(\frac{\partial u_1}{\partial x_2}\right)\left(\frac{\partial u_2}{\partial x_1}\right)} - \left(\widetilde{\frac{\partial u_1}{\partial x_2}}\right)\left(\widetilde{\frac{\partial u_2}{\partial x_1}}\right) \right\rangle \simeq \left\langle \widetilde{\left(\frac{\partial u_2}{\partial x_3}\right)\left(\frac{\partial u_3}{\partial x_2}\right)} - \left(\widetilde{\frac{\partial u_2}{\partial x_3}}\right)\left(\widetilde{\frac{\partial u_3}{\partial x_2}}\right) \right\rangle$$

$$\simeq \left\langle \widetilde{\left(\frac{\partial u_1}{\partial x_3}\right)\left(\frac{\partial u_3}{\partial x_1}\right)} - \left(\widetilde{\frac{\partial u_1}{\partial x_3}}\right)\left(\widetilde{\frac{\partial u_3}{\partial x_1}}\right) \right\rangle. \quad \text{(B2)}$$